Catalysis Science & Technology

ROYAL SOCIETY OF CHEMISTRY

PAPER

Cite this: *Catal. Sci. Technol.*, 2024, **14**, 7107

Elucidation of Ce/Zr ratio effects on the physical properties and catalytic performance of CuO_x/$Ce_yZr_{1-y}O_2$ catalysts†

Mohammed Sifat,[a] Michal Luchowski,[a] Amol Pophali,[a] Wenhui Jiang,[a] Yunfan Lu,[a] Byeongseok Kim,[b] Gihan Kwon,[c] Kwangsuk Yoon,[d] Jihun Kim,[e] Kwangjin An,[e] Sang Eun Shim,[b] Hocheol Song[d] and Taejin Kim *[a]

Although cerium oxide (CeO_2) is widely used as a catalyst support, its limited defect sites and surface oxygen vacancy/mobility should be improved. The incorporation of zirconium (Zr) in the cerium (Ce) lattice is shown to increase the number of oxygen vacancies and improve catalytic activity. Using a fixed surface density (SD) of copper (~2.3 Cu atoms per nm^2) as a surface species, the role of the support ($Ce_yZr_{1-y}O_2$ (y = 1.0, 0.9, 0.6, 0.5, and 0.0)) and defect site effects in the CO oxidation reaction was investigated. Spectroscopic (*e.g.*, Raman, XRD, XPS) and microscopic (*e.g.*, SEM-EDX, HR-TEM) characterization techniques were applied to evaluate the defect sites, crystallite size, lattice parameters, chemical composition, oxidation states of elements and microstructure of the catalysts. The CO oxidation reaction with varied $CO:O_2$ ratios (1 : 5, 1 : 1, and 1 : 0.5 (stoichiometric)) was used as a model reaction to describe the relationship between the structure and the catalytic performance of each catalyst. Based on the characterization results of $Ce_yZr_{1-y}O_2$ materials, the addition of Zr causes physical and chemical changes to the overall material. The inclusion of Zr into the structure of CeO_2 decreased the overall lattice parameter of the catalyst and increased the number of defect sites. The prepared catalysts were able to reach complete CO conversion (~100%) at low temperature conditions (<200 °C), each showing varied reaction activity. The difference in CO oxidation activity was then analyzed and related to the structure, wherein Cu loading, surface oxygen vacancies, reduction–oxidation ability, CuO_x–support interaction and oxygen mobility in the catalyst were the crucial descriptors.

Received 19th August 2024,
Accepted 25th October 2024

DOI: 10.1039/d4cy01012d

rsc.li/catalysis

1. Introduction

Carbon monoxide (CO) is a dangerous pollutant present in air that can be toxic to humans even at very low concentration levels over 50 ppm, while its lethality quickly increases with increasing concentration past 200 ppm.[1,2] Due to its toxicity, the catalytic oxidation of CO has been of great interest to a variety of industries for applications including CO gas sensors, filtration in air-purification devices such as respirators, and automotive pollution control systems.[3] The role of CO in syngas makeup raises continuous concern about CO pollutants available due to biomass-derived processes becoming increasingly more favorable in the recent decades for providing fuel and energy needs.[4] Due to varying concentrations in which CO exists as a pollutant and in reactions, effective oxidation of CO is necessary under varying temperatures and reactant compositions. As such, the need to control CO emissions has become increasingly more apparent throughout the years.

In recent decades, cerium oxide (CeO_2), commonly referred to as ceria, has been widely studied in heterogeneous catalysis due to its high oxygen storage capacity (OSC) and propagation of the Ce^{3+} and Ce^{4+} redox cycle, helping to avoid catalyst deactivation over time.[5–7] It has a face-centered cubic (FCC) structure, and its highly organized lattice network allows for the presence of oxygen vacancies produced by the propagation of redox processes, leading to increased O_2 adsorption used during CO oxidation.[8,9] In addition to CO oxidation, CeO_2-based supports have been

[a] *Materials Science and Chemical Engineering Department, Stony Brook University, Stony Brook, NY, 11794, USA. E-mail: taejin.kim@stonybrook.edu*
[b] *Department of Chemistry and Chemical Engineering, Education and Research Center for Smart Energy and Materials, Inha University, Incheon, 22212, South Korea*
[c] *National Synchrotron Light Source II, Brookhaven National Laboratory, Upton, NY 11973, USA*
[d] *Department of Earth Resources and Environmental Engineering, Hanyang University, Seoul 04763, Republic of Korea*
[e] *School of Energy and Chemical Engineering, Ulsan National Institute of Science and Technology, Ulsan 44919, Republic of Korea*

† Electronic supplementary information (ESI) available. See DOI: https://doi.org/10.1039/d4cy01012d

applied in a range of fields, including ethanol steam reforming (ESR) for hydrogen production, NO reduction by CO for the removal of NO_x pollutants, and reverse water gas shift (RWGS) for the production of syngases.[5,10,11]

Although CeO_2 has been widely employed in various catalytic reactions, it has been reported that pure CeO_2 has a low number of oxygen defect sites and low thermal stability, resulting in limited active sites (or OSC) and low specific surface area (SSA) at higher calcination treatment temperatures.[5,12–14] To modify the physicochemical properties of CeO_2, a secondary metal species (*e.g.*, zirconium (Zr), tin (Sn), titanium (Ti), lanthanum (La)) has been incorporated into the lattice to form $Ce_yM_{1-y}O_2$ solid solutions.[5,15–17] Among $Ce_yM_{1-y}O_2$ materials, Zr-doped CeO_2-based catalysts ($Ce_yZr_{1-y}O_2$) have been extensively studied and used in automotive catalytic converters.[18–21] Compared to CeO_2, $Ce_yZr_{1-y}O_2$ has showed a higher OSC, SSA and oxygen mobility under similar treatment conditions.[22–27] The incorporation of Zr^{4+} in the Ce^{4+} lattice can change the structure due to the smaller ionic radius of Zr^{4+} (0.84 Å) compared to that of Ce^{4+} (0.97 Å), leading to an overall decrease in the lattice parameter of $Ce_yZr_{1-y}O_2$.[22–24,28] X. Yao *et al.* reported that $CuO_x/Ce_yZr_{1-y}O_y$ showed relatively better catalytic performance for NO reduction by CO compared to $CuO_x/Ce_ySn_{1-y}O_x$ and $CuO_x/Ce_yTi_{1-y}O_x$, which can be attributed to the gradient of electronegativity between primary and secondary support metals.[5] Since Zr (1.33) has a lower electronegativity compared to Sn (1.96) and Ti (1.54) in the Ce (1.12)-based solid solution, Cu^{2+} is more likely to gain electrons and become Cu^+ in the $CuO_x/Ce_yZr_{1-y}O_x$ catalyst. Surface Cu species exist in various oxidation states due to direct interaction with the support lattice.[5] As indicated by the redox equilibrium, $Cu^{2+} + Ce^{3+} \leftrightarrow Cu^+ + Ce^{4+}$, the presence of Cu^{2+} (or Cu^+) could affect the amounts of oxygen vacancies and defect sites due to the change of Ce oxidation state (+3 or +4).[5,8] J. Chen *et al.* studied the effect of the Ce/Zr ratio on the catalytic activity for CH_4 combustion reaction and redox properties.[28] The authors reported that $Ni/Ce_{0.83}Zr_{0.17}O_2$ showed the highest catalytic performance as compared to CeO_2, $Ce_{0.17}Zr_{0.83}O_2$ and ZrO_2 supported Ni catalysts due to its high OSC, which increases the defect sites, improving the mobility of oxygen species. P. Biswas and D. Kunzru investigated the ethanol steam reforming (ESR) reaction over a series of $Ce_yZr_{1-y}O_2$ (y = 0, 0.26, 0.59, 0.84 and 1) supported Ni catalysts and concluded that high reducibility and high OSC of catalysts are related to the high catalytic activity and hydrogen selectivity.[11]

It has been reported that platinum group metals (PGMs) have shown high catalytic performance for the CO oxidation reaction. Due to their high cost, however, research has been focused on studying alternative highly active non-PGM catalysts.[11,29–31] L. Zhou *et al.* studied the effect of TMs (*e.g.*, Cu, Co, Ni, Mn, and Fe) on CO oxidation over the TM_xCeO_{2-x} catalyst and reported that Cu_xCeO_{2-x} showed the highest catalytic activity.[30] The authors concluded that the electronic structure and oxygen vacancies are responsible for the higher catalytic activity. It has been reported that TMs increase the catalytic activity due to the formation of surface defects, and the selection of surface TM species is highly dependent on the oxygen vacancy formation energy, E_{vf}, of the metal.[29] Among several TMs, Cu has been shown to have a lower E_{vf}, leading to increased catalytic activity for the CO oxidation reaction.[32,33] The addition of a surface species and a secondary metal on the CeO_2 lattice is seen to increase the OSC, catalytic activity, and oxygen vacancies.[34,35]

Although CeO_2 supported TMO_x catalysts have been studied extensively; to understand the support effect (or interaction between surface species and support), fixing the surface density (SD, number of surface metal atoms per nm^2) should be considered. In the present work, a series of $CuO_x/Ce_yZr_{1-y}O_2$ catalysts ($CeO_2:ZrO_2$ = 90 : 10, 60 : 40, and 50 : 50 by weight percent) were prepared with a fixed Cu SD. The fixed SD of Cu on the supports allows for the number of copper atoms per given area of support (~2.3 Cu atoms per nm^2) to be similar for each catalyst. This allows for studying the direct effect of the CeO_2/ZrO_2 ratio on the catalytic activity. To measure the catalytic performance of the synthesized catalysts, CO oxidation as a model reaction was performed: $CO + \frac{1}{2} O_2 \rightarrow CO_2$. A variety of spectroscopic and microscopic characterization techniques, such as ICP, BET, Raman, XRD, SEM-EDX and TEM, were employed to determine the molecular structure of the supports and supported catalysts. It was found that the incorporation of Zr into the Ce lattice increases the defect sites. However, the catalytic performance was not proportional to the increase in defect sites. It was also observed that increasing the O_2 feed concentration hinders the activity of the catalysts, with oxygen vacancies playing a larger role under leaner O_2 feed conditions.

2. Experimental section

2.1 Materials and catalyst preparation

$Ce_yZr_{1-y}O_2$ (y = 1.0, 0.9, 0.6, 0.5, 0.0) materials were provided by Daiichi Kigenso Kagaku Kogyo (DKK). The preparation of the catalysts involved proprietary company methods using a combination of hydrolysis and co-precipitation methods for formation of various $CeO_2:ZrO_2$ mixed-oxide ratios (9 : 1, 6 : 4, 5 : 5 by weight percent). The precursors used for synthesis of the mixed-oxide catalysts were a combination of cerium(IV) hydroxide ($Ce(OH)_4$) and zirconium(IV) oxychloride ($ZrOCl_2$).

Copper(II) acetylacetonate ($Cu(acac)_2$, $Cu(C_5H_7O_2)_2$, ≥99.9% trace metals basis) was purchased from Sigma-Aldrich. The $CuO_x/Ce_yZr_{1-y}O_2$ (SD = ~2.3 Cu atoms per nm^2) samples were synthesized by a one-pot chemical vapor deposition (OP-CVD) method as shown in Fig. 1. The OP-CVD method followed three steps for catalyst synthesis: (I) pre-mixing: $Ce_yZr_{1-y}O_2$ and $Cu(acac)_2$ were added to a mortar and mixed for 15 min. The mixed powder was transferred to an aluminum oxide boat (Sigma-Aldrich), and then the sample was transported into a tubular furnace (Lindberg/Blue M Tube Furnace, model number TF55030A-1). (II) Dispersion: the transported sample was treated at 155 °C for 2 hours

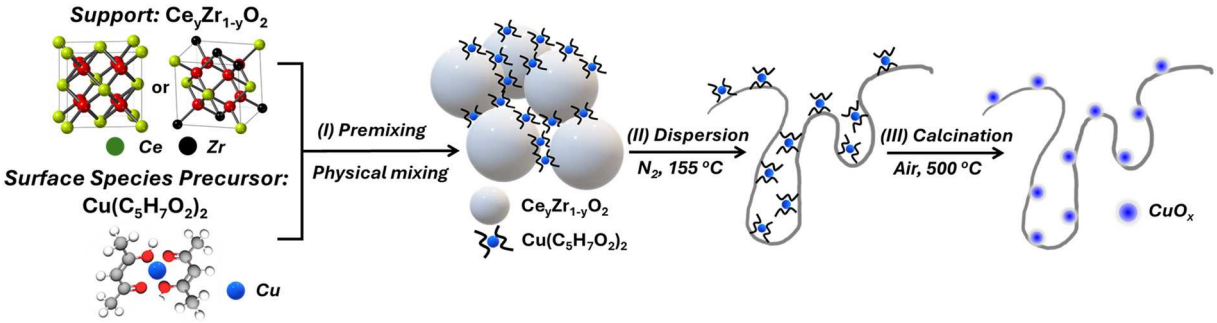

Fig. 1 Scheme of the synthesis of copper oxide (CuO_x) on $Ce_yZr_{1-y}O_2$ (y = 1.0, 0.9, 0.6, 0.5, 0.0) supports.

under flowing N_2 gas (Airgas, ultra-high-purity N_2) at a rate of 20 mL min^{-1}. Dispersion temperature conditions were selected using a programmed-TGA method in which the 10% weight loss region of the precursor was determined. (III) Calcination: following the dispersion, air (Airgas, dry air: 20% O_2 and 80% N_2) flowing at a rate of about 25 mL min^{-1} was used to calcine the sample at 500 °C for 4 hours. The synthesized $CuO_x/Ce_yZr_{1-y}O_2$ catalyst was left to cool overnight at room temperature and sieved (500 μm, Fieldmaster) to ensure a uniform particle size.

2.2 Catalyst characterization

For the X-ray diffraction (XRD) analysis, the $Ce_yZr_{1-y}O_2$ catalysts underwent synchrotron X-ray diffraction (S-XRD) (λ = 0.1665 Å) measurement. The processing of the data for conversion from two-dimensional (2D) high energy scattering patterns to one-dimensional (1D) data was done using Dioptas software. The $CuO_x/Ce_yZr_{1-y}O_2$ supported catalysts underwent lab scale XRD using an X'Pert powder diffractometer (PANalytical) with a Cu-Kα radiation source (λ = 1.5406 Å) operating at 40 kV and 30 mA. The measurement was performed with a diffraction angle 2θ range of 20°–80° at a scanning speed of 1.33° min^{-1}. The Raman spectra of the $Ce_yZr_{1-y}O_2$ and $CuO_x/Ce_yZr_{1-y}O_2$ catalysts were obtained with visible (532 nm, Horiba Xplora Plus Raman microscope) and UV (325 nm, Renishaw inVia™ Raman microscope) excitation at room temperature and ambient pressure. The obtained spectra were displayed within a Raman shift (cm^{-1}) range of 100 to 2000 cm^{-1}, with spectral acquisition scanning parameters set to 10 accumulations at 10 s per scan. The elemental compositions and associated oxidation states were determined by testing the catalysts using X-ray photoelectron spectroscopy (XPS, Thermo Scientific K-Alpha) with monochromatic Al-Kα radiation ($h\nu$ = 1486.6 eV). The obtained data were analyzed for XPS fitting using Origin software with a Tougaard method baseline and Voigt method curve fitting. N_2 adsorption–desorption isotherm curves were obtained at 77 K (−196 °C) using a Micromeritics ASAP 2020 instrument. Prior to the N_2 adsorption–desorption procedures, the samples were degassed at 300 °C for 4 hours for removal of any impurities or moisture. The specific surface areas (SSAs) were calculated by the multipoint Brunauer–Emmett–Teller (BET) method. The pore size distribution and the average pore volume of the catalysts were determined by the Barrett, Joyner, and Halenda (BJH) method. Scanning electron microscopy coupled with energy dispersive X-ray (SEM-EDX) analysis was carried out on an EmCrafts Cube II scanning electron microscope (voltage 10 kV). Samples were attached to a specimen holder with carbon tape and coated with platinum. The microstructure of the synthesized catalysts was investigated using transmission electron microscopy (TEM; JEOL, HEM-2100F). The samples were thoroughly dispersed in ethyl alcohol (~1.5 mg ml^{-1}) and then mounted on a Ni grid. This sample-mounted Ni grid was further dried under ambient conditions and then used for the measurement. Inductively coupled plasma-optical emission spectrometry (ICP-OES, Optima 5300DV, PerkinElmer) was used to determine the Cu loading. Prior to the ICP-OES measurement, 0.02 g of the sample was dissolved in 10 mL of nitric acid (70% HNO_3) using a microwave digestion system (ETHOS TC, Milestone).

2.3 Catalytic activity test

The CO oxidation reaction was carried out in a quartz packed bed reactor (inner diameter (ID) = 7 mm, outer diameter (OD) = 9.6 mm) and 40 mg of the catalyst was used. The total flow rate was kept consistent between various activity tests to achieve a gas hourly space velocity (GHSV) value of 75 000 ml h^{-1} g_{cat}^{-1}. The sample was pretreated with flowing He (30 mL min^{-1}, Airgas, ultra-high purity) at 500 °C (ramping rate of 5 °C min^{-1} from room temperature) for 30 min. Following the pretreatment procedure, the temperature was cooled to room temperature and the gas composition was switched to the desired reactant compositions. The total flow rate was 50 mL min^{-1} and the feed gases were varied with different CO-to-O_2 ratios: (I) 20 mL min^{-1} CO (Airgas, 10% CO with balance He), 10 mL min^{-1} O_2 (Airgas, ultra-high purity), and 20 mL min^{-1} He (Airgas, ultra-high-purity) for the 1 : 5 CO-to-O_2 ratio, (II) 20 mL min^{-1} CO, 2 mL min^{-1} O_2, and 28 mL min^{-1} He for the 1 : 1 CO-to-O_2 ratio, and (III) 40 mL min^{-1} CO, 2 mL min^{-1} O_2, and 8 mL min^{-1} He for the 1 : 0.5 CO-to-O_2 ratio (stoichiometric). The reactants and products were analyzed by using an online gas chromatograph (GC, Trace 1300 gas chromatograph, Thermo Scientific) containing a capillary

column (Carboxen® 1010 PLOT) equipped with a thermal conductivity detector (TCD).

3. Results

3.1 Characterization of structural properties

To determine the surface morphology and the elemental distribution of the $CuO_x/Ce_yZr_{1-y}O_2$ catalysts, SEM-EDX mapping was performed (Fig. 2). The surface of the CuO_x/CeO_2 catalyst is relatively smooth compared to other samples (Fig. 2(a)). As the Zr loading increased, the surface of the catalyst became rougher, and more clusters were observed (Fig. 2(b–e)). Furthermore, with the increase in Zr loading, the grain size of $CuO_x/Ce_{0.6}Zr_{0.4}O_2$, $CuO_x/Ce_{0.5}Zr_{0.5}O_2$, and CuO_x/ZrO_2 became smaller, and the surface morphology of the catalysts seemed to resemble more closely that of CuO_x/ZrO_2. The elemental mapping results show that copper oxides were well dispersed uniformly for each of the synthesized samples.

The TEM results demonstrate that the CuO_x species were present on the surface of the respective supports as shown in Fig. 3. Low-magnification TEM images of the catalysts are presented in Fig. 3(a–e), where particle overlap was observed. To investigate the microstructural characteristics of the catalyst materials, high-magnification TEM images (Fig. 3(a′–e′)) were collected. The presence of constituent species (CeO_2, CuO_x, and ZrO_2) in each catalyst was confirmed based on the interplanar distance corresponding to the catalyst's composition. A consistent

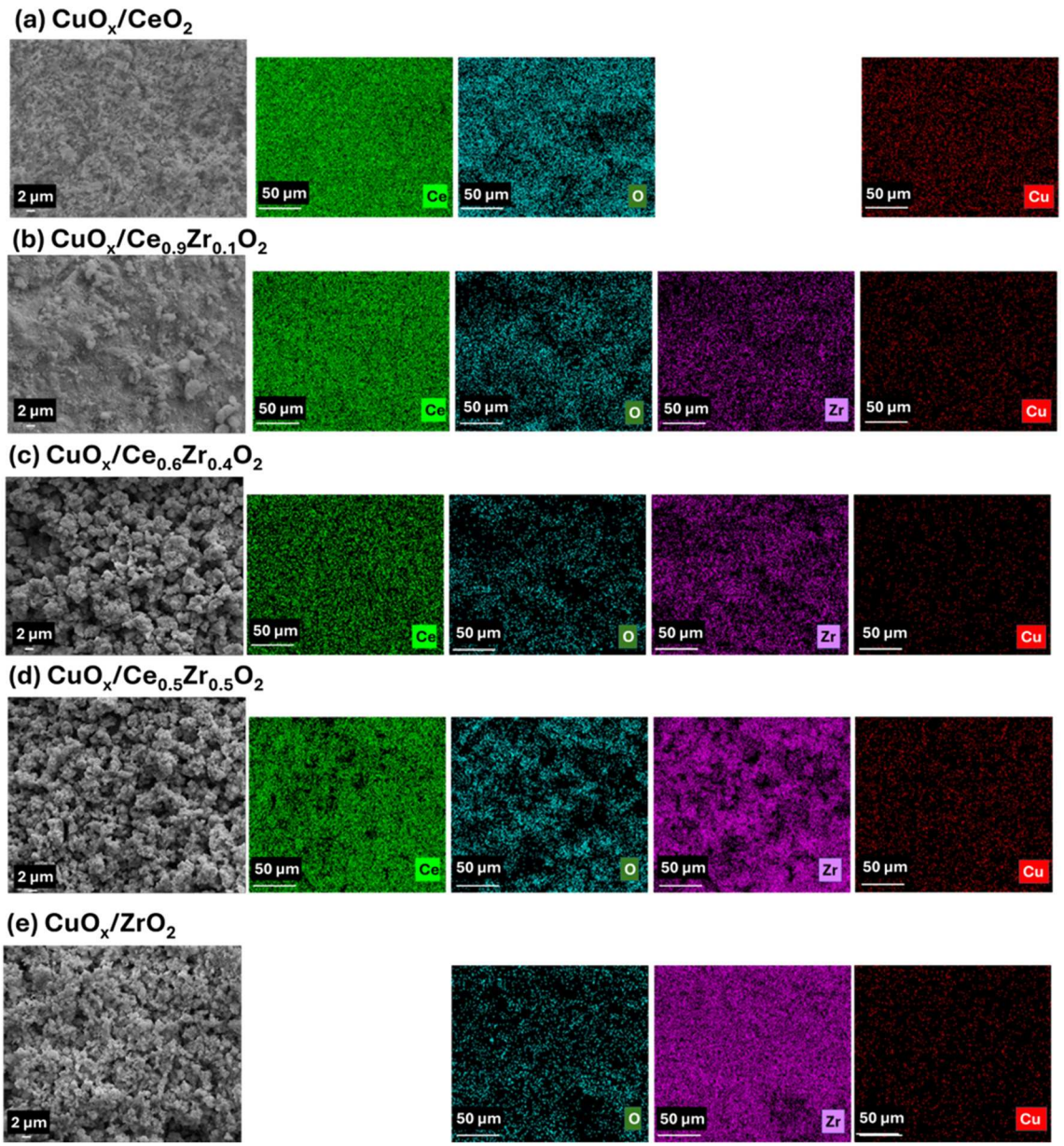

Fig. 2 SEM-EDX analysis images of (a) CuO_x/CeO_2, (b) $CuO_x/Ce_{0.9}Zr_{0.1}O_2$, (c) $CuO_x/Ce_{0.6}Zr_{0.4}O_2$, (d) $CuO_x/Ce_{0.5}Zr_{0.5}O_2$, and (e) CuO_x/ZrO_2.

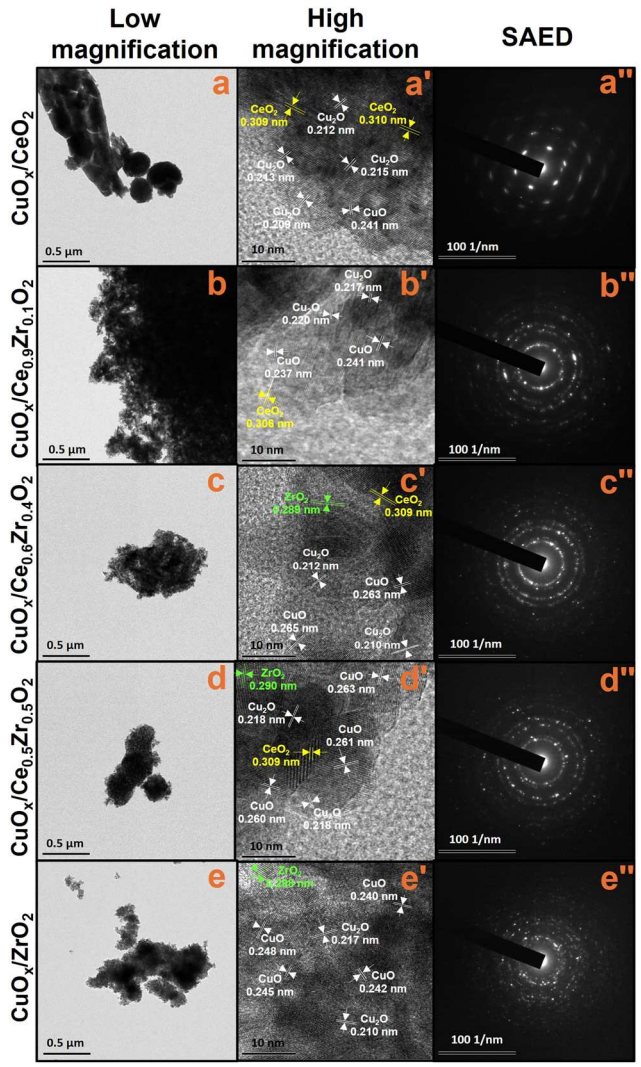

Fig. 3 High-resolution TEM (HR-TEM) images of the synthesized catalysts: (a–a″) CuO_x/CeO_2, (b–b″) $CuO_x/Ce_{0.9}Zr_{0.1}O_2$, (c–c″) $CuO_x/Ce_{0.6}Zr_{0.4}O_2$, (d–d″) $CuO_x/Ce_{0.5}Zr_{0.5}O_2$, and (e–e″) CuO_x/ZrO_2. High-magnification images (a′–e′) indicate lattice spacing of metal species (in nm).

lattice spacing of ~0.309 nm, corresponding to the (111) plane of CeO_2, was observed in both CuO_x/CeO_2 and CuO_x/CZ catalysts.[36] Although the lattice spacing of CeO_2 is expected to be influenced by Zr contents, no noticeable expansion or contraction of the CeO_2 lattice was observed in the HR-TEM results. Different types of the dispersed CuO_x species were identified, revealing the presence of CuO (Cu^{2+}) and Cu_2O (Cu^{1+}) in CuO_x/CeO_2, CuO_x/CZ and CuO_x/ZrO_2 catalysts, with corresponding lattice spacing of 0.240–0.265 and 0.209–0.220 nm, respectively.[37,38] Lattice fringes for ZrO_2 (0.290–0.298 nm) were detected in all Zr-containing catalysts except for $CuO_x/Ce_{0.9}Zr_{0.1}O_2$, where the higher CeO_2 content likely obscured the ZrO_2 fringe patterns.[39,40] Additionally, the SAED pattern seen in Fig. 3(a″) indicates a highly crystalline lattice (dotted pattern) structure for the CeO_2-based catalyst.[41] However, with increasing Zr content in the support, the SAED patterns (Fig. 3(b″–e″)) appeared hazy, corroborating the increasing disorder in the catalyst structure.[41]

Table 1 Specific surface area (SSA) for $Ce_yZr_{1-y}O_2$ (y = 1.0, 0.9, 0.6, 0.5, 0.0) supports and $CuO_x/Ce_yZr_{1-y}O_2$ (y = 1.0, 0.9, 0.6, 0.5, 0.0) catalysts

Sample (support)	S_{BET} ($m^2\ g^{-1}$)	Molar ratio (Ce : Zr)	Sample (supported)	S_{BET} ($m^2\ g^{-1}$)
CeO_2	125.7	1 : 0	CuO_x/CeO_2	115.1
$Ce_{0.9}Zr_{0.1}O_2$	71.2	1 : 0.16	$CuO_x/Ce_{0.9}Zr_{0.1}O_2$	70.6
$Ce_{0.6}Zr_{0.4}O_2$	57.1	1 : 0.92	$CuO_x/Ce_{0.6}Zr_{0.4}O_2$	55.2
$Ce_{0.5}Zr_{0.5}O_2$	53.2	0.72 : 1	$CuO_x/Ce_{0.5}Zr_{0.5}O_2$	50.0
ZrO_2	108.2	0 : 1	CuO_x/ZrO_2	101.4

N_2 adsorption and desorption allow for the calculation of the SSA and pore size distribution (or pore volume) of a material. The determined SSA for each of the $Ce_yZr_{1-y}O_2$ supports (Table 1) shows a decreasing SSA with an increase in Zr content, while bulk ZrO_2 contains a higher SSA than that of $Ce_yZr_{1-y}O_2$. In the case of the $CuO_x/Ce_yZr_{1-y}O_2$ supported catalysts' SSA, a similar trend can also be observed. Since the synthesized samples' SSAs were similar to those of the supports, a minimal change is expected in the surface area following the dispersion and calcination of CuO_x on the support. Based on the pore diameter distributions and the type IV isotherm curves, it was determined that the synthesized catalysts had a mesoporous structure (Fig. 4(a) and (b)).[42] It is worth noting that $Ce_{0.9}Zr_{0.1}O_2$ shows a very different N_2 adsorption–desorption type with a higher pore diameter compared to other $Ce_yZ_{1-y}O_2$ samples. Even if the $Ce_{0.9}Zr_{0.1}O_2$ composition (Ce : Zr molar ratio = 1 : 0.16) is similar to CeO_2, the results were not comparable. Furthermore, although the $CuO_x/Ce_{0.9}Zr_{0.1}O_2$ sample's SSA value is similar to that of $CuO_x/Ce_{0.6}Zr_{0.4}O_2$ and $CuO_x/Ce_{0.5}Zr_{0.5}O_2$, its physical properties could be different.

ICP-OES characterization was used to identify the atomic composition of each of the samples and confirm the deposition of Cu on each of the samples. The target SD of Cu for each of the samples was fixed at a value of 2.3 Cu atoms per nm^2 based on a 3.0 wt% Cu loading basis on pure CeO_2 support. The SD value was initially fixed using the equation:

$$\mathrm{SD}\left(\text{atoms per nm}^2\right) = \frac{\frac{W_{\mathrm{Cu}}}{100}\left(\mathrm{g}\right) \times 6.02 \times 10^{23}\ \left(\text{atoms per mol}\right) \times \frac{1}{M_{\mathrm{Cu}}}\left(\text{mol g}^{-1}\right)}{\mathrm{SSA_{supp}}\ \left(\text{m}^2\ \text{g}^{-1}\right) \times \left(1 - \frac{W_{\mathrm{Cu}}}{100}\right)\left(\mathrm{g}\right) \times 10^{18}\left(\text{nm}^2\ \text{m}^{-2}\right)} \quad (1)$$

where W_{Cu} is the weight loading percent of Cu, M_{Cu} is the molar mass of Cu (63.5 g mol^{-1}), and SSA_{supp} is the SSA of the respective support material (Table 1). The SDs of the synthesized catalysts were confirmed using the equation:

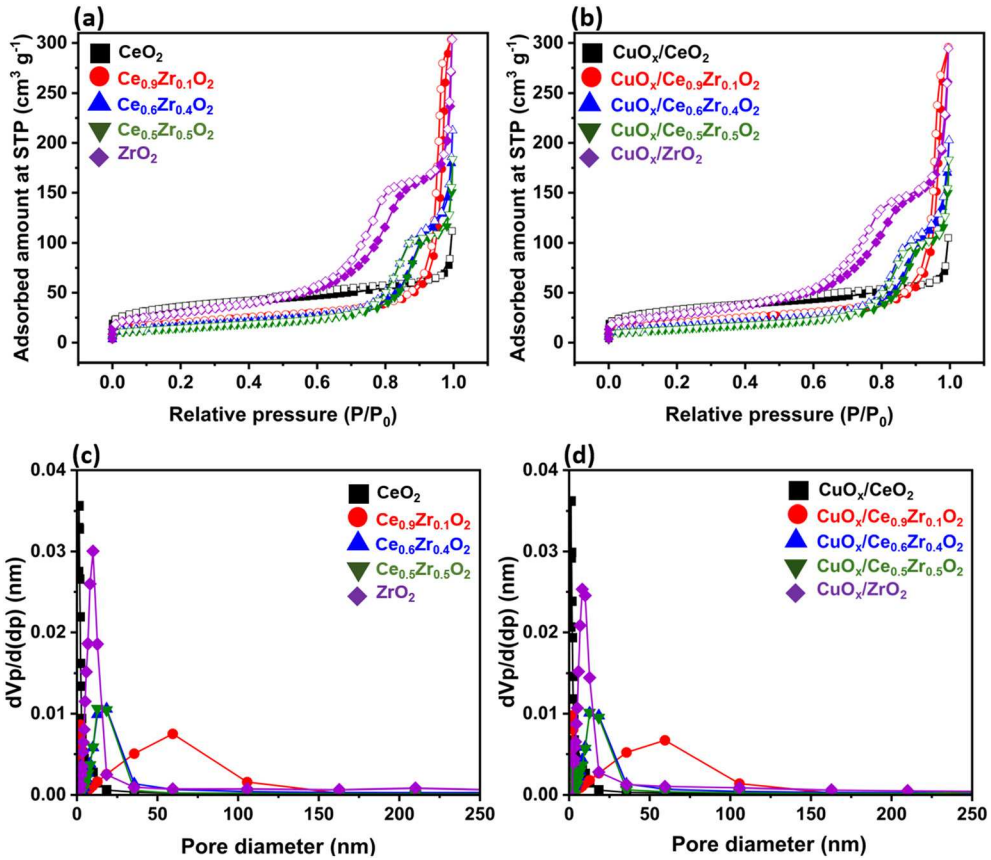

Fig. 4 N_2 adsorption and desorption plots for (a) $Ce_yZr_{1-y}O_2$ (y = 1.0, 0.9, 0.6, 0.5, 0.0) supports and (b) $CuO_x/Ce_yZr_{1-y}O_2$ (y = 1.0, 0.9, 0.6, 0.5, 0.0) catalysts. BJH pore size distribution for (c) $Ce_yZr_{1-y}O_2$ (y = 1.0, 0.9, 0.6, 0.5, 0.0) and (d) $CuO_x/Ce_yZr_{1-y}O_2$ (y = 1.0, 0.9, 0.6, 0.5, 0.0) catalysts.

$$\mathrm{SD}\left(\text{atoms per nm}^2\right) = \frac{\frac{W_{\mathrm{Cu}}}{100}\left(\mathrm{g}\right) \times 6.02 \times 10^{23}\left(\text{atoms per mol}\right) \times \frac{1}{M_{\mathrm{Cu}}}\left(\text{mol g}^{-1}\right)}{\mathrm{SSA}_{\mathrm{synth}}\left(\mathrm{m}^2\ \mathrm{g}^{-1}\right) \times 10^{18}\left(\mathrm{nm}^2\ \mathrm{m}^{-2}\right)} \tag{2}$$

where SSA_{syth} is the SSA of the synthesized catalyst (Table 1).

As indicated in Table 2, all samples had comparable SDs of ~2.0 Cu atoms per nm^2, indicating controllable Cu precursor adsorption and its dispersion onto each support with varied Cu loadings (*e.g.*, 1.0–3.0 wt%). These results also provide that CeO_2, $Ce_yZr_{1-y}O_2$, and ZrO_2 are effective support materials for Cu species' dispersion using the current synthesis method.

Raman spectroscopy is a powerful analytical tool that provides information about molecular vibrations by measuring the inelastic scattering of light. Visible (532 nm) Raman spectroscopy was used to analyze the $Ce_yZr_{1-y}O_2$-based support and $CuO_x/Ce_yZr_{1-y}O_2$ materials and the collected spectra are presented in Fig. S1.† For comparison, CeO_2 and ZrO_2 Raman spectra were also collected. Please note that the CeO_2 and $Ce_yZr_{1-y}O_2$ spectra were normalized with respect to the F_{2g} band to better distinguish the formation and relative intensity change of other peaks (Fig. S1(a)†). Bulk ZrO_2 contains peaks at 107, 183, 335, 384, 480, 561, and 615 cm^{-1} Raman shift, representing the monoclinic

Table 2 ICP-OES results with a comparison of desired and actual surface densities of catalysts

Sample	Theoretical Cu loading (wt%)	Actual Cu loading[a] (wt%)	Theoretical SD (Cu atoms per nm^2)	Actual SD[b] (Cu atoms per nm^2)
CuO_x/CeO_2	3.0	2.6	2.3	2.1
$CuO_x/Ce_{0.9}Zr_{0.1}O_2$	1.7	1.4	2.3	1.9
$CuO_x/Ce_{0.6}Zr_{0.4}O_2$	1.4	1.1	2.3	1.9
$CuO_x/Ce_{0.5}Zr_{0.5}O_2$	1.3	1.0	2.3	1.8
CuO_x/ZrO_2	2.6	2.1	2.3	2.0

[a] ICP results. [b] Applying the SSA of the synthesized catalysts from Table 1.

phase of zirconia.[43] For CeO_2, $Ce_{0.9}Zr_{0.1}O_2$, $Ce_{0.6}Zr_{0.4}O_2$ and $Ce_{0.5}Zr_{0.5}O_2$, their Raman spectra show a high-intensity peak at ~463 cm^{-1}, which is ascribed to the F_{2g} vibration due to the fluorite-type lattice structure of the varying CeO_2-based samples.[44–48] As the Zr content increased, the F_{2g} peak was slightly shifted to a higher Raman shift (or blue shift) from 463 cm^{-1} to 467 cm^{-1}. Since Zr^{4+} has a smaller ionic radius than Ce^{4+}, the Zr–O bonding is shorter and stronger than Ce–O bonding, causing contraction in the structure and resulting in a blue shift.[43] In addition to a peak shift, $Ce_{0.6}Zr_{0.4}O_2$ and $Ce_{0.5}Zr_{0.5}O_2$ show a relatively broadened F_{2g} peak shape compared to CeO_2 and $Ce_{0.9}Zr_{0.1}O_2$ peaks due to the contribution of the 480 cm^{-1} Zr peak. Moreover, the presence of a peak at 141 cm^{-1} and 144 cm^{-1} in the bulk support as well as $CuO_x/Ce_{0.6}Zr_{0.4}O_2$ and $CuO_x/Ce_{0.5}Zr_{0.5}O_2$ (Fig. S1(b)†), respectively, indicates a transition of the ZrO_2 structure from monoclinic (m) to tetragonal (t) due to the incorporation of a larger amount of Zr in the CeO_2 lattice.[49,50] This is followed by a broad peak in the 500–620 cm^{-1} range, indicating the changes of extrinsic (D_{ex}) and intrinsic (D_{in}) defect sites.[51–53] It was reported that intensity variations of D_{ex} and D_{in} are caused by the addition of dopants and changing of the inherent structure of the material, respectively.[51–53] This result confirms the increasing of defect sites with increasing Zr loading on the CeO_2 structure. In the case of the CuO_x/support samples, the Raman spectra are similar to that of the bulk support ones, indicating a well-dispersed Cu surface species on the respective supports. Please note that CuO_x Raman peaks, which appear around the 150, 290–350, and ~600 cm^{-1} regions in general, were either not observed or were overlapped by the defect region of the supports.[54–58] The defect regions, especially for CuO_x/CeO_2 and $CuO_x/Ce_{0.9}Zr_{0.1}O_2$, exhibit an increase in intensity following the addition of Cu, indicating an increase in defect regions within the structure of the catalyst.[53] Additionally, compared to bulk CeO_2, the CuO_x/CeO_2 sample shows the F_{2g} peak's broadness as well as a shift to a lower wavenumber, while other CuO_x/support samples show similar results to their support spectra. This is likely a result of the changes in the CeO_2 lattice due to thermal treatment of the support during CuO_x/CeO_2 synthesis, caused by expansion of the CeO_2 structure.[59–62]

UV (325 nm) Raman spectroscopy is a particularly useful characterization technique for studying defect sites in catalysts, and the collected data are shown in Fig. 5.[63] The UV Raman data shown in Fig. 5(a) indicate the presence of the F_{2g} band of CeO_2 within the $Ce_yZr_{1-y}O_2$ samples at around 461–467 cm^{-1}. The defects in the CeO_2 structure are indicated with peaks at <~600 cm^{-1} in both bulk CeO_2 and $Ce_{0.9}Zr_{0.1}O_2$ supports. The CeO_2 defect region can be seen to increase as the Zr ratio increased as well as the disappearance of the F_{2g} band (*e.g.*, $Ce_{0.5}Zr_{0.5}O_2$).[64,65] The spectra also show a second-order longitudinal optical band (2LO) of CeO_2 at ~1200 cm^{-1} following a similar trend to the defect peaks as they also experienced a blue shift with increased amounts of Zr in the ratio. The blue shifts in the F_{2g} band as well as increasing of the defect sites with increasing Zr ratio clearly indicate a structural change.[66,67] Similar to the visible Raman spectra, the absence of CuO_x related peaks, as shown in Fig. 5(b), of the CuO_x/support samples indicates a well-dispersed Cu surface species on the respective supports.

As shown in Fig. 6(a) and (b), the CuO_x/support samples exhibit the same diffraction peaks as their bulk support counterparts. For comparison purposes, the lab-scale XRD 2θ values were used for labeling throughout the study for structure identification. It should be noted that there are no apparent CuO_x-related diffraction 2θ values that correspond to 36°, 38°, 44.6°, 57.7°, and 68.5° (Fig. 6(b)), indicating that the CuO_x surface species was well dispersed on the synthesized catalysts. This result also provided a minimal deviation in the lattice structure of CuO_x/support materials when compared to the respective supports.[68–71] The CeO_2 sample showed diffraction peaks at about 28.5°, 33°, 47.5°, 56.4° and 58° with crystal planes corresponding to the (111), (200), (220), (311) and (222) planes, respectively, indicating a

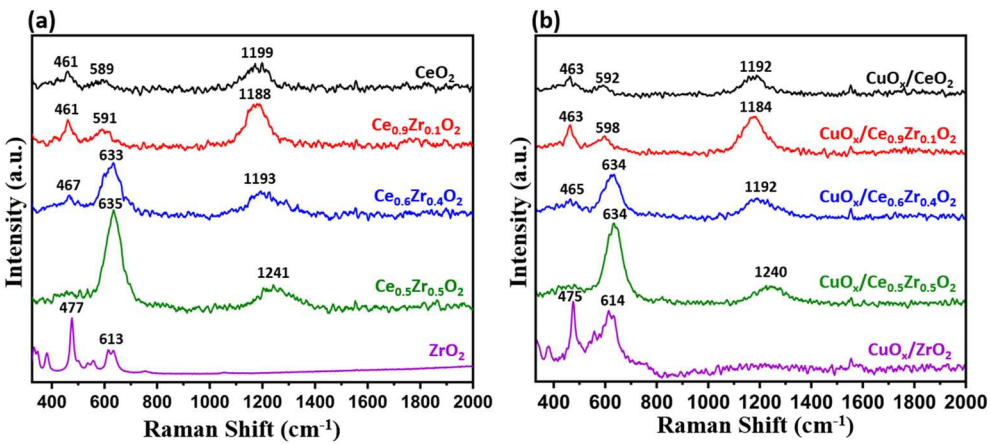

Fig. 5 UV (λ = 325 nm) Raman spectroscopy of (a) $Ce_yZr_{1-y}O_2$ (y = 1.0, 0.9, 0.6, 0.5, 0.0) supports and (b) $CuO_x/Ce_yZr_{1-y}O_2$ (y = 1.0, 0.9, 0.6, 0.5, 0.0) catalysts.

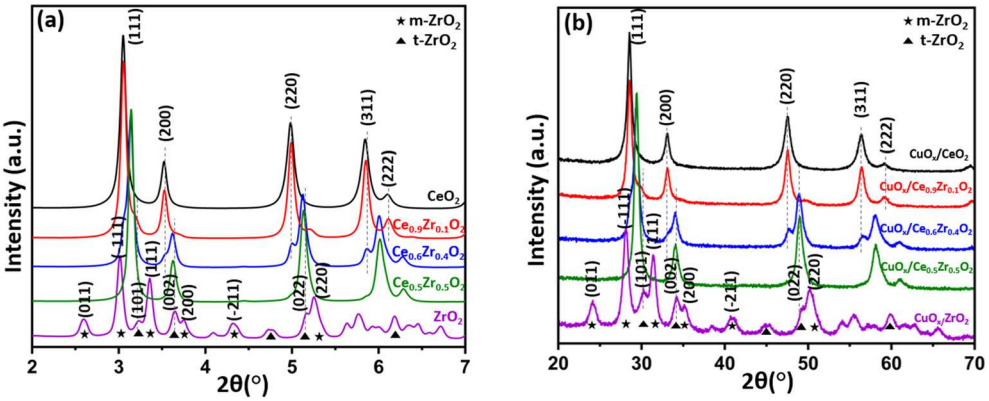

Fig. 6 (a) S-XRD spectra of $Ce_yZr_{1-y}O_2$ (y = 1.0, 0.9, 0.6, 0.5, 0.0) supports (λ = 0.1665 Å) and (b) XRD spectra of $CuO_x/Ce_yZr_{1-y}O_2$ (y = 1.0, 0.9, 0.6, 0.5, 0.0) catalysts (λ = 1.54 Å).

face-centered cubic (FCC) structure.[72–74] Both the bulk ZrO_2 and the CuO_x/ZrO_2 catalyst contain a multiphase structure: monoclinic zirconia (m-ZrO_2) at 24°, 28°, 31.5°, 35.1°, 40.7°, 50.2° and tetragonal phase of zirconia (t-ZrO_2) at 30.2°, 34.5°, 45°, 49.4°, 60°.[75–79] In the case of the $Ce_yZr_{1-y}O_2$ and $CuO_x/Ce_yZr_{1-y}O_2$ samples, CeO_2 related peaks were slightly shifted to a higher angle, while those of both $Ce_{0.9}Zr_{0.1}O_2$-based samples were closest to that of CeO_2-based samples due to the least amount of Ce replacement by Zr in the total ratio. A small shoulder appears at ~30.2°, indicating the presence of t-ZrO_2 in the $Ce_{0.9}Zr_{0.1}O_2$ support and $CuO_x/Ce_{0.9}Zr_{0.1}O_2$ catalyst. Compared to CeO_2 and $Ce_{0.9}Zr_{0.1}O_2$-based samples, the diffraction peaks of $Ce_{0.6}Zr_{0.4}O_2$ and $CuO_x/Ce_{0.6}Zr_{0.4}O_2$ samples were broader, resulting in decreasing crystallite size (Table 3). In addition to peak broadness, the intensities of CeO_2 peaks decreased, while t-ZrO_2 peaks' intensities were increased. The t-ZrO_2 phase becomes more prominent at higher Zr loading as seen with both $Ce_{0.5}Zr_{0.5}O_2$ and $CuO_x/Ce_{0.5}Zr_{0.5}O_2$ samples' XRD patterns. Compared to the $Ce_{0.6}Zr_{0.4}O_2$-based samples, $Ce_{0.5}Zr_{0.5}O_2$-based samples do not show the peak splitting of CeO_2 (200) in addition to disappearance of the (220) and (311) planes of CeO_2. Crystallite size and lattice parameter calculations were from the measured XRD data and using eqn (3) and (4) (see the ESI†). No notable trend of crystallite size can be observed with the change of Ce : Zr ratios as they generally remain in the 10.1–14.1 nm range. However, the lattice parameters were decreased with increasing Zr content in $Ce_yZr_{1-y}O_2$ samples due to the smaller size of the Zr cation than that of the Ce one.

Table 3 Lattice parameter and crystallite size of bulk supports and synthesized catalysts

Sample	FWHM (°)	Lattice parameter (Å)	Crystallite size (nm)
CeO_2	0.074	5.41	11.6
$Ce_{0.9}Zr_{0.1}O_2$	0.071	5.41	12.1
$Ce_{0.6}Zr_{0.4}O_2$	0.076	5.27	11.3
$Ce_{0.5}Zr_{0.5}O_2$	0.062	5.25	13.9
ZrO_2	0.080	4.93	10.7
CuO_x/CeO_2	0.828	5.41	12.3
$CuO_x/Ce_{0.9}Zr_{0.1}O_2$	0.816	5.41	12.2
$CuO_x/Ce_{0.6}Zr_{0.4}O_2$	0.977	5.26	11.1
$CuO_x/Ce_{0.5}Zr_{0.5}O_2$	0.724	5.26	14.1
CuO_x/ZrO_2	0.955	4.93	10.1

The XPS plots of the associated species in $CuO_x/Ce_yZr_{1-y}O_2$ (y = 1.0, 0.9, 0.6, 0.5, 0.0) are presented in Fig. 7. The core level Ce 3d spectrum was observed in the 870–930 eV range (Fig. 7(a–e)) and consisted of Ce $3d_{3/2}$ and Ce $3d_{5/2}$ bands. The Ce 3d spectra observed for CuO_x/CeO_2, $CuO_x/Ce_{0.9}Zr_{0.1}O_2$, $CuO_x/Ce_{0.6}Zr_{0.4}O_2$ and $CuO_x/Ce_{0.5}Zr_{0.5}O_2$ were deconvoluted into a total of 10 peaks. The peaks (in blue) observed at ~880.1, ~882.5, ~899.2, and ~903.5 eV correspond to Ce^{3+} species.[80–83] The peaks (in red) observed at ~882.4, ~888.9, ~898.3, ~900.7, ~907.5, and ~916.7 eV are attributed to the Ce^{4+} species.[80–83] The content of Ce^{3+} (relative to Ce^{4+}) was obtained by comparison of their respective peak areas determined by using eqn (3):

$$\%\,[Ce^{3+}] = \frac{[Ce^{3+}]}{[Ce^{3+}] + [Ce^{4+}]} \quad (3)$$

where $[Ce^{3+}]$ and $[Ce^{4+}]$ are the cumulative peak areas of Ce^{3+} and Ce^{4+}, respectively.[82] As shown in Table 4, the % $[Ce^{3+}]$ values in the CuO_x/CZ samples (0.16–0.19) were slightly higher than in the CuO_x/CeO_2 sample (0.13), although there was minimal variation with changing Zr concentration. The presence of Cu is confirmed in all $CuO_x/Ce_yZr_{1-y}O_2$ catalysts with the presence of Cu 2p bands in the 920–960 eV range. The deconvoluted Cu 2p spectra are presented in Fig. 7(a′–e′). At a glance, the peaks at ~933.9, ~941.2 and ~953.9 eV are assigned to Cu^{2+} species, while the peaks at ~932.3 and ~952.2 eV correspond to Cu^{1+} species.[81,84] To determine the percentage of dominant Cu oxidation state on the catalyst surface, a relative area calculation was performed using eqn (4) and the obtained values are provided in Table 4.

$$\%\,[Cu^{1+}] = \frac{[Cu^{1+}]}{[Cu^{1+}] + [Cu^{2+}]} \quad (4)$$

In eqn (4) $[Cu^{1+}]$ and $[Cu^{2+}]$ are the cumulative peak areas of Cu^{1+} and Cu^{2+}, respectively. A decrease in Cu^{1+} content was

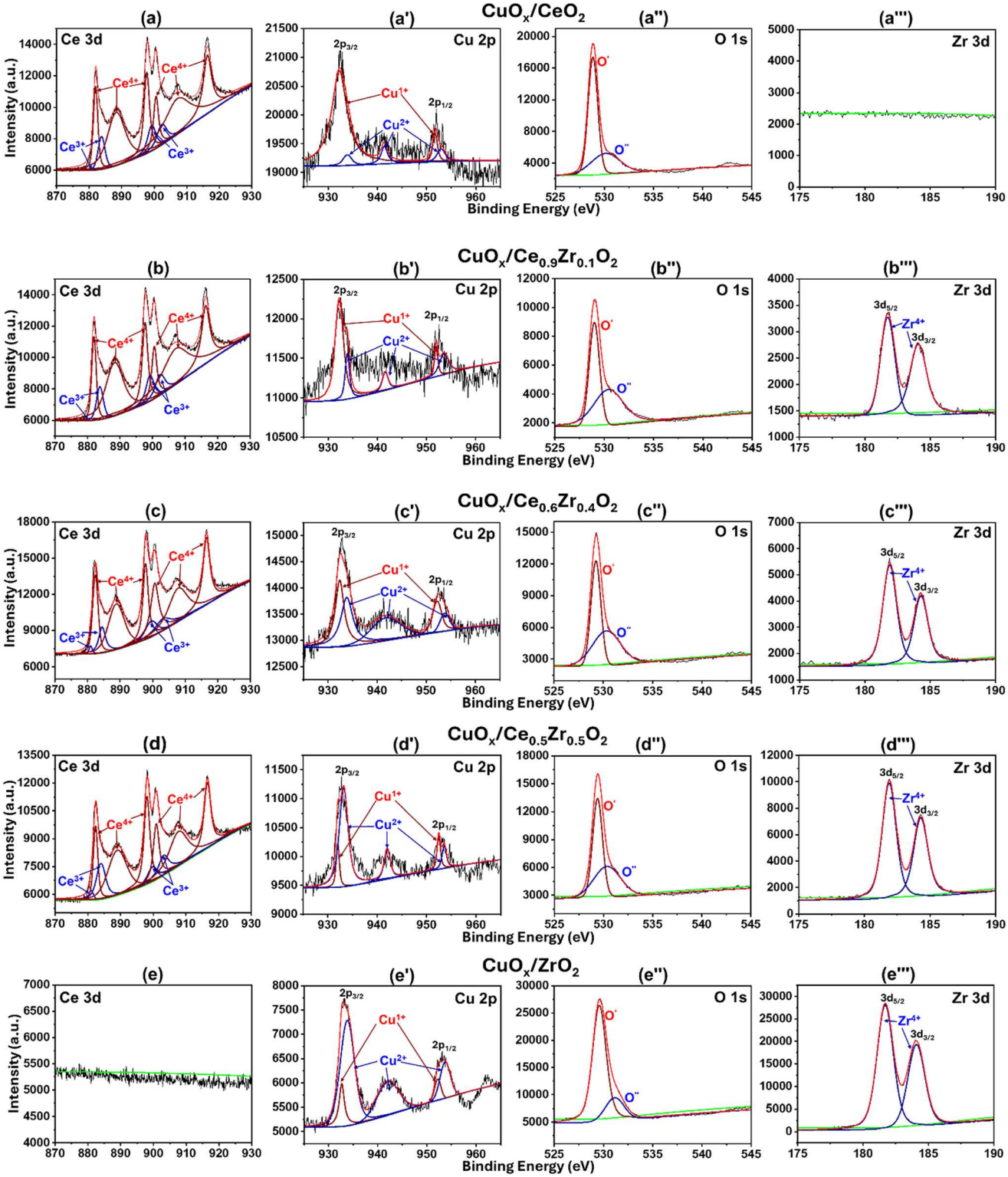

Fig. 7 XPS results for $CuO_x/Ce_yZr_{1-y}O_2$ (y = 1, 0.9, 0.6, 0.5, 0) showing deconvolution over (a–e) Ce 3d, (a′–e′) Cu 2p, (a″–e″) O 1s, and (a‴–e‴) Zr 3d spectra.

observed in CuO_x/CeO_2, CuO_x/CZ, and CuO_x/ZrO_2 catalysts with increasing Zr concentration, confirming the relationship between Cu oxidation state and the Ce : Zr ratio. Furthermore, the presence of oxygen was observed in all samples with sharp O 1s spectra in the range of 526–535 eV. Fig. 7(a″–e″) show the deconvoluted peaks in the O 1s spectrum of samples. The peak that appears at ~528.8 eV represents the lattice oxygen (O′) bound to metal species, while the peak at ~530.1 eV is

Table 4 Ce^{3+} area percent, ratio of oxygen vacancies to oxygen in the lattice (O″/O′), and Cu^{1+} area percent

Sample	% [Ce^{3+}]	% [Cu^{1+}]	O″/O′
CuO_x/CeO_2	0.13	0.84	0.52
$CuO_x/Ce_{0.9}Zr_{0.1}O_2$	0.19	0.65	1.08
$CuO_x/Ce_{0.6}Zr_{0.4}O_2$	0.16	0.41	0.95
$CuO_x/Ce_{0.5}Zr_{0.5}O_2$	0.19	0.19	0.83
CuO_x/ZrO_2	—	0.14	—

attributed to loss of oxygen species or creation of oxygen vacancies (defect sites) (O″).[80,85] The area ratio of oxygen-related peaks (O″/O′) provides insights into the presence of oxygen vacancies in the catalyst. Similar to the % [Ce^{3+}] results, the CuO_x/CZ catalysts (0.83–1.08) exhibited a higher O″/O′ ratio than CuO_x/CeO_2 (0.52), indicating a higher presence of oxygen vacancies. The Zr 3d spectra were observed for CuO_x/CZ and CuO_x/ZrO_2 samples in the 178–188 eV range, as shown in Fig. 7(a‴–e‴). The peaks at ~181.7 and ~184.1 eV for Zr^{4+} were attributed to Zr $3d_{5/2}$ and Zr $3d_{3/2}$, respectively.[86,87]

3.2 Catalytic activity testing

Fig. 8 displays the effect of the supports and CO : O_2 feed ratios (*e.g.*, oxygen-rich and stoichiometric conditions) on the CO conversion as a function of temperature. It is evident that CuO_x/CeO_2 and $CuO_x/Ce_{0.9}Zr_{014}O_2$ show a higher catalytic performance than other samples under different CO : O_2 ratios based on its T_{20}, T_{50}, and T_{90} values (Fig. 9(a–c) and Table S1†). For instance, the CuO_x/CeO_2 and $CuO_x/Ce_{0.9}Zr_{0.1}O_2$ catalysts achieved a T_{20} of 51.8 °C and 69.3 °C, respectively, under CO : O_2 (1 : 5) conditions, while $CuO_x/Ce_{0.6}Zr_{0.4}O_2$ (93.6 °C), $CuO_x/Ce_{0.5}Zr_{0.5}O_2$ (127.6 °C), and CuO_x/ZrO_2 (141.5 °C) catalysts show higher T_{20} temperatures under the same reaction conditions. In addition to the support effect, it was also observed that CO : O_2 ratios affect the CO oxidation over the tested catalysts. In the case of CuO_x/CeO_2 and $CuO_x/Ce_{0.9}Zr_{0.1}O_2$ catalysts, their catalytic performance was slightly decreased (increasing T_{20}, T_{50} and T_{90} temperatures) with decreasing O_2/CO ratio (CO : O_2 = 1 : 1 and 1 : 0.5) (Fig. S2 and Table S1†). However, the opposite trend can be seen with the $CuO_x/Ce_{0.6}Zr_{0.4}O_2$ and $CuO_x/Ce_{0.5}Zr_{0.5}O_2$ catalysts, as their catalytic performance shows an increase with decreasing O_2/CO ratios (Fig. 9(d)). A similar trend was also observed with the CuO_x/ZrO_2 catalyst. The $CuO_x/Ce_{0.6}Zr_{0.4}O_2$ and $CuO_x/Ce_{0.5}Zr_{0.5}O_2$ catalysts achieved their lowest T_{20} values (88.8 °C and 92.2 °C, respectively) under stoichiometric (lean O_2) feed conditions. Interestingly, under stoichiometric conditions, 100% CO conversion was not achieved as shown in Fig. 8(c), indicating a possible competition between the filling in of oxygen vacancies and the propagation of the

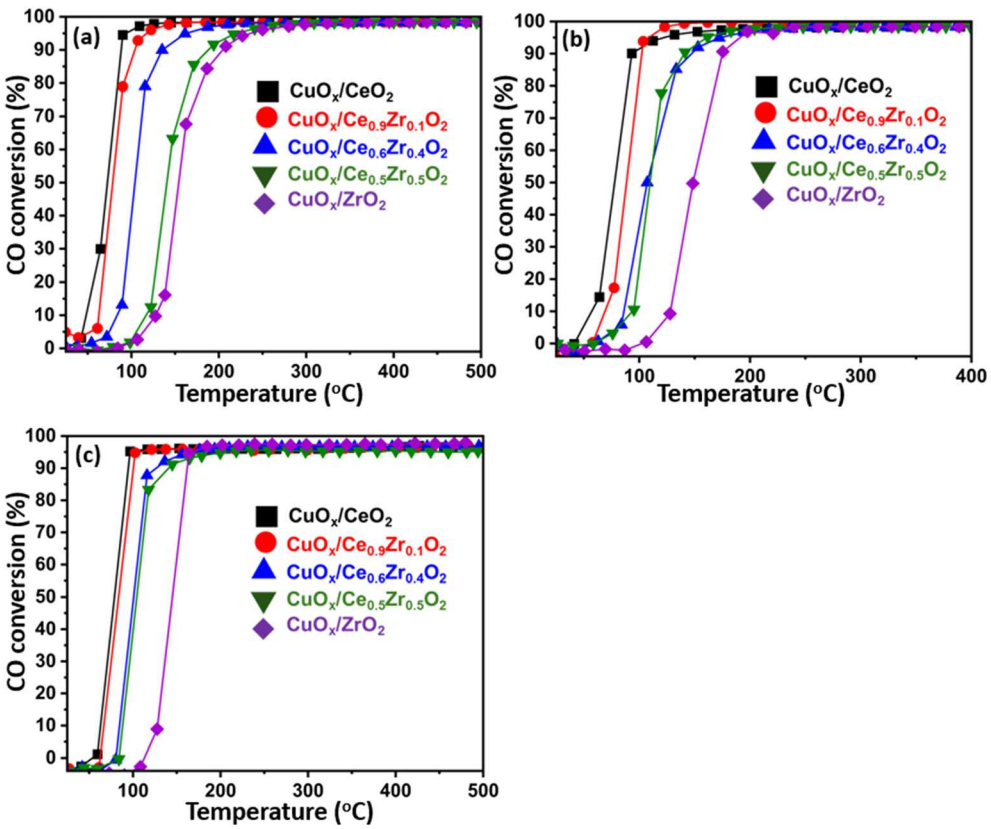

Fig. 8 CO oxidation tests over $CuO_x/Ce_yZr_{1-y}O_2$ (y = 1.0, 0.9, 0.6, 0.5, 0.0) catalysts with CO : O_2 feed ratios of (a) 1 : 5, (b) 1 : 1, and (c) 1 : 0.5 (stoichiometric conditions).

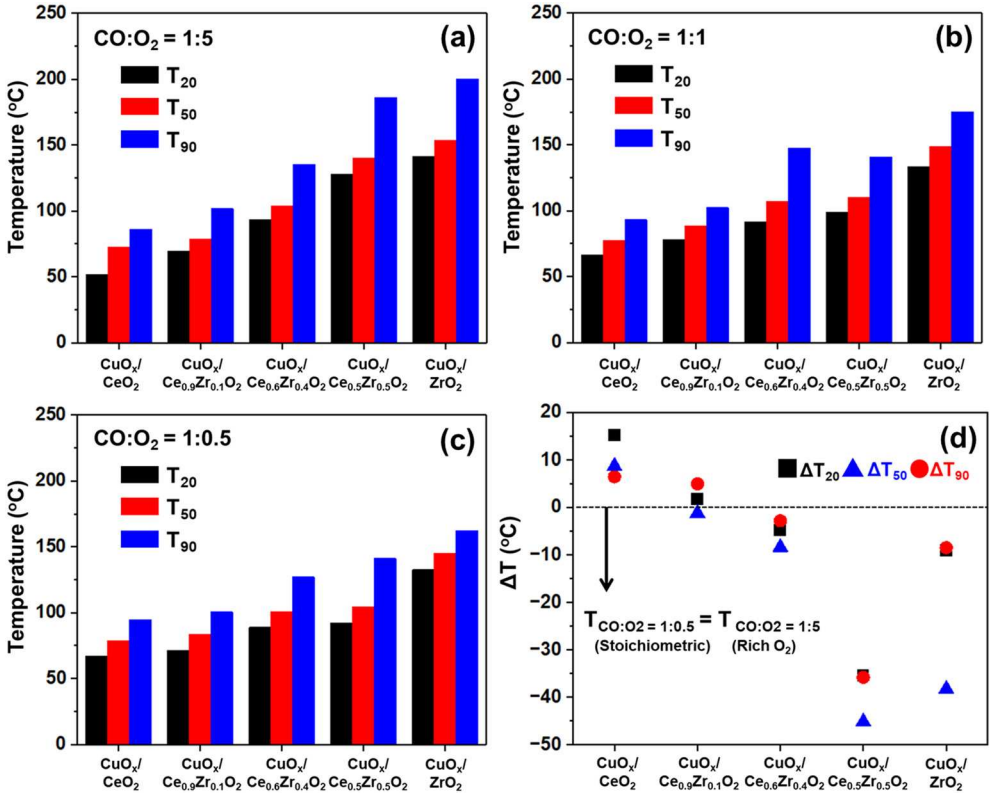

Fig. 9 T_{20}, T_{50}, and T_{90} for $CuO_x/Ce_yZr_{1-y}O_2$ (y = 1.0, 0.9, 0.6, 0.5, 0.0) catalysts; $CO:O_2$ feed ratios of (a) 1 : 5, (b) 1 : 1, and (c) 1 : 0.5 (stoichiometric conditions). (d) ΔT for $CuO_x/Ce_yZr_{1-y}O_2$ catalysts, where $\Delta T = T_{T_{20},T_{50},T_{90}}$ at $CO:O_2$=1:0.5 − $T_{T_{20},T_{50},T_{90}}$ at $CO:O_2$=1:5.

reaction. In short, for each flow condition, a consistent trend is observed in the sample activity: CuO_x/CeO_2 > $CuO_x/Ce_{0.9}Zr_{0.1}O_2$ > $CuO_x/Ce_{0.6}Zr_{0.4}O_2$ > $CuO_x/Ce_{0.5}Zr_{0.5}O_2$ > CuO_x/ZrO_2.

4. Discussion

4.1 The effect on CeO_2 structure with Zr loading

The incorporation of Zr into the CeO_2 lattice influences the overall structure of the material. The lattice parameters (Table 3) calculated from the XRD plot have a downward trend with increasing Zr loading, indicating that Zr has been successfully incorporated into the catalyst support structure. The downward trend of the overall lattice parameter for each support as the Zr percentage increases was due to the replacement of Ce^{4+} by a smaller ionic radius Zr^{4+}.[22–24,28,43] The diffraction peaks of $Ce_{0.5}Zr_{0.5}O_2$ have the relatively highest angle shift as compared to CeO_2 among the diffraction patterns of all different ratio samples due to the highest amount of Ce replacement by Zr in the catalyst structure (Fig. 6(a)). The higher angle shift of the Zr-containing $Ce_yZr_{1-y}O_2$ samples indicates a contraction of the lattice of the material due to increased loading of Zr.[22–24,88–90] The appearance of a shoulder near both 5° and 50° in the $Ce_{0.6}Zr_{0.4}O_2$ respective support and supported catalyst diffraction patterns indicates a transitional state in the ZrO_2 structure to a combination of monoclinic and tetragonal phases of CeO_2 and ZrO_2 based on loading ratio.[91–94] Additionally, the appearance of a peak at 34.5° corresponding to t-ZrO_2 in the $Ce_{0.6}Zr_{0.4}O_2$ and $Ce_{0.5}Zr_{0.5}O_2$ catalysts indicates a shift in the lattice structure of the CeO_2-based catalysts. The UV Raman data (Fig. 5) also indicate a shift in the F_{2g} and 2LO peaks of the samples with increasing Zr loading, which indicates the integration of ZrO_2 into the CeO_2 structure.[90,95,96] The decrease in the F_{2g} as well as the 2LO band intensity with increasing Zr content can indicate a shift from a CeO_2-dominant structure to a modified CeO_2 structure caused by the contraction of the lattice following the addition of Zr.[90,92,95,96] Focusing on the F_{2g} band on the visible Raman plot (Fig. S1(a)†), it is noted that it shifts closer to the right (blue shift) near the 480 cm^{-1} peak of m-ZrO_2 with increasing Zr ratio, confirming a decrease in bond length because of the stronger bond strength of Zr^{4+} compared to Ce^{4+}.[97] The reduced bond length further supports the shrink in overall size as indicated by the calculated lattice parameters of the samples (Table 3).[88–90] The broad defect band between 500 cm^{-1} and 620 cm^{-1} is an indication of increased amounts of extrinsic and intrinsic defect sites on the support, affected by both increasing Zr loading and the addition of a CuO_x dopant (Fig. S1(b)†).[51–53] For both the bulk and the supported $Ce_{0.5}Zr_{0.5}O_2$ samples, the peaks in the defect range are of higher intensities compared to that of $Ce_{0.6}Zr_{0.4}O_2$ and $Ce_{0.9}Zr_{0.1}O_2$, indicating that there is an increase in defect sites within the $Ce_yZr_{1-y}O_2$

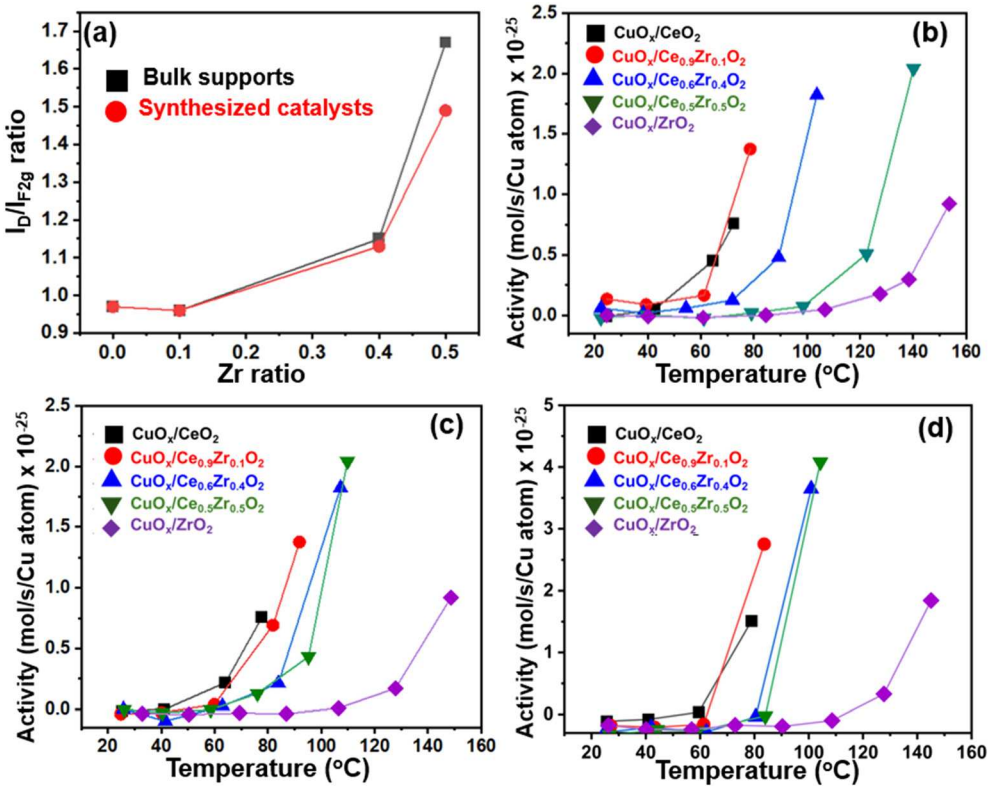

Fig. 10 (a) Ratios of the peak intensities of the defect region (I_D) and the F_{2g} mode ($I_{F_{2g}}$). Activity plots (mol s^{-1} per Cu atom) for CO oxidation tests for $CuO_x/Ce_yZr_{1-y}O_2$ (y = 1.0, 0.9, 0.6, 0.5, 0.0) catalysts; the activity plots were calculated for $CuO_x/Ce_yZr_{1-y}O_2$ catalysts undergoing CO oxidation with $CO:O_2$ feed ratios of (b) 1 : 5, (c) 1 : 1, and (d) 1 : 0.5 (stoichiometric conditions) and data displayed up to T_{50}.

catalyst supports at higher Zr loadings. The change in $I_D/I_{F_{2g}}$ ratios (Fig. 10(a)) from the UV Raman spectra of the catalysts further indicates that the ratio increases with increasing Zr loading while remaining generally the same between bulk and synthesized catalysts. The intensity of the defects increases while the intensity of the F_{2g} peak decreases, indicating increased amounts of defects in the samples with increased Zr loading and the defect peak becoming dominant. The distinction between extrinsic and intrinsic defects is less clear than in the visible Raman spectra, but the overall presence of defects can be determined by comparison of the loss in ceria's F_{2g} character of the material with increasing defects due to increased addition of Zr into the CeO_2 lattice.

The surface characterization results obtained from XPS measurements were analyzed. While UV Raman, a bulk technique, confirmed the increase in defect sites with increasing Zr content, the surface characteristics from XPS provided further insights. In this context, Ce^{3+}, Cu^{1+} and O″ are indicative of the chemistry over the surface of the catalysts. The CuO_x/CeO_2 sample also exhibited the highest % [Cu^{1+}] and lowest % [Ce^{3+}] among the prepared catalysts. As indicated by the O″/O′ ratio in Table 4, the inclusion of Zr led to an increase in defect sites. However, the redox equilibrium varied for each catalyst. The generation of Cu^{1+} species (from Cu^{2+}) is driven by the higher electronegativity of Cu compared to Ce, facilitating electron acceptance to attain redox mechanism: $Ce^{3+} + Cu^{2+} \leftrightarrow Cu^{1+} + Ce^{4+}$. The defect sites and oxygen mobility also contribute towards the generation of Ce^{3+} and Cu^{1+}. The authors hypothesize that the availability of % [Cu^{1+}] is crucial for oxidation reactions to maximize redox properties.

4.2 The role of oxygen vacancies on activity

As shown by the CO conversion data (Fig. 8), CuO_x/CeO_2 has the highest performance in oxygen-rich environments due to the innate redox capabilities of Ce^{3+} and Ce^{4+} that increase its oxygen mobility.[5–7,12–14] With initial fixed SDs of 2.3 Cu atoms per nm^2, all the synthesized $CuO_x/Ce_yZr_{1-y}O_2$ samples have comparable resulting SDs within the range of ~2.0 Cu atoms per nm^2, with the highest resulting SD samples being the catalysts with the highest Ce loading. The slightly higher resulting actual SD values of CuO_x/CeO_2 and $CuO_x/Ce_{0.9}Zr_{0.1}O_2$ can be due to the higher SSA of the respective bulk supports compared to the other supports, except for bulk ZrO_2 also resulting in an increased overall activity.[75] As shown in Fig. 10(b–d), when normalized by the number of Cu atoms, the highest activity (mol s^{-1} per Cu atom), which was obtained at low CO conversion (<20% CO conversion), is achieved by the CuO_x/CeO_2 and $CuO_x/Ce_{0.9}Zr_{0.1}O_2$ catalysts. Please note that the near doubling in activity of the catalysts shown in Fig. 10(d) under stoichiometric feed ratios of reactants can be explained by the increase of CO

concentration during excess O_2 feed conditions from 4% to 8% to keep the space velocity of the reaction consistent. The relatively low catalytic performance of the CuO_x/ZrO_2 catalyst can be attributed to the lower inherent OSC of ZrO_2 and lack of a redox cycle compared to that of CeO_2-based materials.[21–24] Additionally, an improvement in the performance of Zr-based catalysts can be seen with increasing Ce loading due to improved acid–base support properties compared to that of a pure ZrO_2 support.[21–24] This allows for the proceeding of the reaction with ample optimized interactions with the support. The catalysts achieved a lower final conversion value of ~97% at stoichiometric feed ratios (seen in Fig. 8(c)) due to the competition between O_2 and CO reactants in the feed and filling in of produced vacancies in the lattice, resulting in O_2 becoming the limiting reactant.[34,35,98] As such, both CuO_x/CeO_2 and $CuO_x/Ce_{0.9}Zr_{0.1}O_2$ catalysts obtained the highest relative conversions under low temperature conditions with varied feed conditions.

To further account for the difference in catalytic activity between the catalysts with a relatively constant number of Cu active sites, the role of oxygen vacancies within the structures of each catalyst during the reaction must be considered. As shown by the CO oxidation activity tests at various excess O_2-feed conditions, oxygen vacancies seem to have less of a role as increasingly excess O_2 reactants can lead to the vacancies becoming filled in by the excess oxygen in the reactant stream.[9,13,14,21,35,96,98] The catalytic ability of the synthesized catalysts is therefore dependent on the nature of the support and the SSA of the catalyst as well as availability of active sites. In this case, pure CuO_x/CeO_2 has a significantly larger surface area compared to the other supports, resulting in more active copper sites even under similar SD conditions (Tables 1 and 2), leading to better overall conversion at lower temperatures. In contrast, increasing content of Zr in the support leads to a shift in the CO conversion temperatures to the higher temperatures, indicating an increase in the relative T_{20}, T_{50} and T_{90} (Fig. 9 and S2†). It could be hypothesized that as the Zr content increases, the catalyst's performance decreases due to a lower surface area and the high rate of the oxygen vacancies refilling during the reaction in the presence of O_2 reactants.[29,35,75] Although the oxygen vacancies in the catalysts increase with higher Zr concentrations in the $Ce_yZr_{1-y}O_2$ catalyst, these vacancies could serve as (1) adsorption sites for reactants and (2) catalytic activity sites. In the case of low SSA catalysts, however, especially in oxygen-rich conditions, the high kinetics of the filling of these vacancies by O_2 leads to a slow regeneration rate, resulting in reducing the number of active sites available for CO oxidation. Consequently, CO conversion in high-Zr-ratio $CuO_x/Ce_yZr_{1-y}O_2$ catalysts (*e.g.*, $CuO_x/Ce_{0.6}Zr_{0.4}O_2$ and $CuO_x/Ce_{0.5}Zr_{0.5}O_2$) results in lower catalytic performance.[21,35,96,98] The combination of the lower SSA and the reduction of active sites on the catalyst can explain why the activity of Zr-promoted supported catalysts is lower compared to that of CuO_x/CeO_2. As a result, the oxygen defect sites in $Ce_yZr_{1-y}O_2$ supported catalysts may not be as efficient as desired, depending on the reactant feed ratios (O_2 lean or O_2 rich) of the reaction in which they are used. To increase the efficiency of the catalytic reaction, it is important to create a catalyst that satisfies both high SSA and abundant OSC.

As described in section 2.1 and shown in Table 2, the catalyst synthesis was based on calculations for a constant Cu surface density (SD = ~2.3 Cu atoms per nm^2). Table 2 confirms both the actual Cu loading (wt%) and SD. Previous studies reported that the CO oxidation reaction occurs at the interface between CuO_x and CeO_2 or CeO_2–ZrO_2 support.[99] In this study, the highest Cu loading was obtained in CuO_x/CeO_2, resulting in greater availability of interfaces, which facilitated CO conversions at lower temperatures. During the reaction, oxygen mobility enhances the metal–support interaction necessary for continuous redox properties, with oxygen vacancies acting as driving potholes for this movement. As shown in Fig. 5, the inclusion of ZrO_2 creates oxygen vacancies or defects in the catalyst. However, an increase in defects does not always enhance catalytic activity, and the lower oxygen mobility of ZrO_2 compared to CeO_2 may negatively affect catalytic activity. A study by M. Piumetti *et al.* reveals that an optimal balance Ce and Zr content is necessary in the catalyst to achieve sufficient oxygen mobility and create oxygen vacancies, both of which positively influence CO oxidation and help attain the required activity.[100] A higher availability of oxygen vacancy is not the sole factor contributing to an effective catalytic reaction. As shown in Fig. 8(c) and 9(c), $CuO_x/Ce_{0.9}Zr_{0.1}O_2$ shows comparable activity with a stoichiometric feed ratio, despite having a Cu loading (1.4 wt%) that is nearly half of that in CuO_x/CeO_2 (2.6 wt%). This explains the positive impact of the incorporation of ZrO_2 into the CeO_2 structure. With an increase in the oxygen level in the feed, the activity of CuO_x/CeO_2 and $CuO_x/Ce_{0.9}Zr_{0.1}O_2$ improved. However, a decrease in activity was observed for $CuO_x/Ce_{0.6}Zr_{0.4}O_2$, $CuO_x/Ce_{0.5}Zr_{0.5}O_2$, and CuO_x/ZrO_2 catalysts as the O_2/CO_2 ratio increased in the feed. This behavior could be attributed to two main reasons: structural and mechanistic considerations. Firstly, the structural characterization of $CuO_x/Ce_{0.6}Zr_{0.4}O_2$ and $CuO_x/Ce_{0.5}Zr_{0.5}O_2$ shows an increase in defects as the cerium content decreases. This results in causing reduced oxygen mobility and fewer surface redox-active centers. The second factor is mechanistic, where CO oxidation primarily occurs through the activation of metal centers by oxygen from the feed, which subsequently adsorbs the gas phase CO for CO_2 formation.[101] With increased oxygen in the feed, the adsorption of CO at the activated site becomes less favorable due to the higher concentration of oxygen molecules in the vicinity. As a result, higher temperatures are required for effective CO adsorption and to facilitate CO_2 formation. This is validated by Fig. 8 and 9, where the breakthrough and subsequent conversion

points were observed at higher temperatures as the O_2: CO ratio increased.

The XPS results revealing the presence of the Cu^{1+} and Ce^{3+} species (Fig. 7 and Table 4) in the catalysts correlate with the observed activity results. Higher values of Cu^{+1} and lower values of Ce^{3+} tend to create a gradient that influences the equilibrium mechanism (Ce^{3+} + Cu^{2+} ⟷ Cu^{1+} + Ce^{4+}) based on the availability of these species. For example, CuO_x/CeO_2 exhibits a higher concentration of surface Cu^{1+}, which enhances its oxidation capacity. This shift will drive the redox equilibrium backwards upon oxidation, continuously balancing the species throughout the reaction. Consequently, this mechanism is proposed as a source of synergistic effect that enhances CO oxidation performance.

The creation of bulk defects and surface oxygen vacancies has been explained through Raman spectroscopy (Fig. 5 and S1†) and XPS analysis (Fig. 7), respectively. Additionally, the presence of lattice distortion was evident from HR-TEM results. The varying electronic states of Cu (Cu^{1+} and Cu^{2+}) were clearly explained in the HR-TEM (Fig. 3) and XPS (Fig. 7) results. The observed results provide that these electronic states contribute to charge-transfer interaction between Cu and the CeO_2-based support's lattice at their interface.[102–104] The presence of Cu^{1+} can be seen in all but the CuO_x/CeO_2 catalyst, which is in agreement with the presence of a low concentration of Ce^{3+} as shown by the XPS data in Fig. 7. The addition of CuO_x increases the reduction–oxidation ability of the support, which is influenced primarily by the composition of $Ce_yZr_{1-y}O_2$. This is supported by the inverse relationship observed between the Ce^{3+} and Cu^{1+} ratios (Table 4). During the CO oxidation reaction, this phenomenon can assist in the adsorption of CO onto the activated CuO_x surface species, which subsequently interacts with lattice oxygen at the metal–support interface, reducing the surface species and creating oxygen vacancies.[103,104] The support composition plays a critical role in determining the type and strength of metal–support interaction.[103–105] An *et al.* reported that the nature of surface species is key to the effectiveness of metal–support interaction in the CO oxidation reaction.[103–105] Therefore, metal/metal oxide–support interactions contribute towards increase of the overall active sites for the propagation of the reaction. In this study, the inclusion of Zr up to ~10% constructively contributes to CO oxidation activity. However, the CuO_x/CeO_2 catalyst showed superior activity among the tested samples due to its higher metal loading, better redox properties, favorable metal oxide–support interactions, and facilitated oxygen mobility under varying feed conditions.

5. Conclusions

A series of CuO_x/$Ce_yZr_{1-y}O_2$ (y = 1.0, 0.9, 0.6, 0.5, 0.0) catalysts with similar SD (number of Cu atoms per nm^2) values were prepared by OP-CVD. Raman and XRD analyses confirmed that surface CuO_x species were well dispersed on the supports. CuO_x/CeO_2 showed the highest catalytic activity (mol s^{-1} per Cu atom) for the CO oxidation reaction, followed by CuO_x/$Ce_{0.9}Zr_{0.1}O_2$. An improvement in overall CO conversion with higher SSA was observed, even though the number of oxygen defect sites/supports showed inverse trends. The effective distribution and presence of CuO_x over $Ce_yZr_{1-y}O_2$ supports were confirmed from the microstructural data obtained from HR-TEM data. The oxidation states of associated elements in the catalysts were determined using XPS measurements. An indirect quantification of Cu^{1+}, Ce^{3+} and surface oxygen vacancies (O″) were analyzed from the deconvolution of the XPS data. The role of oxygen vacancies (both extrinsic and intrinsic) due to the incorporation of a Zr promoter was studied during reaction under varying O_2 feed conditions, in which materials with the highest number of defects performed considerably worse under excess O_2 feeds. Under the O_2-rich environment, the quantity of metal centers, surface oxygen vacancies, reduction–oxidation ability, metal oxide–support interaction and oxygen mobility play a major role in CO oxidation activity. To further investigate the intrinsic differences of these catalysts and reaction conditions, kinetic experiments for determining activation energy (E_a), pre-exponential factors, rate-determining step (RDS) and order of reaction shall be studied separately as an extended scope of this research. To facilitate application in various catalysis industries in addition to fundamental catalysis research, modifications of commercially available supporting materials (*e.g.*, CeO_2 and $Ce_yZr_{1-y}O_2$) should be thought about. Specifically, synthesizing a high-SSA support material with high surface oxygen vacant sites and improved oxygen mobility should be taken into consideration.

Data availability

All data included in this study are available upon request from the corresponding author.

Author contributions

M. Sifat: investigation, formal analysis, writing – original draft, writing – review & editing. M. Luchowski: investigation, formal analysis, writing – original draft, writing – review & editing. A. Pophali: investigation, formal analysis. W. Jiang: investigation, formal analysis, writing – original draft. Y. Lu: investigation, formal analysis, writing – original draft. B. Kim: investigation, methodology, formal analysis. G. Kwon: investigation, methodology, formal analysis. K. Yoon: investigation, formal analysis. J. Kim: investigation, methodology, formal analysis. K. An: supervision. S. E. Shim: supervision. H. Song: supervision. T. Kim: supervision, writing – original draft, writing – review & editing, project administration, funding acquisition. All authors have given approval to the final version of the manuscript.

Conflicts of interest

There are no conflicts of interest to declare.

Acknowledgements

The authors acknowledge funding support from the National Science Foundation (NSF-CBET-2050824). The authors would also like to acknowledge the Advanced Energy Research and Technology Center (AERTC) for the facilities at Stony Brook University. This research used the 28-ID-1 beamline of the National Synchrotron Light Source II, a U.S. Department of Energy (DOE) Office of Science User Facility operated for the DOE Office of Science by Brookhaven National Laboratory under Contract No. DE-SC0012704.

References

1 D. N. Bateman, *Medicine*, 2003, **31**, 41–42.
2 C. L. Townsend and R. L. Maynard, *Occup. Environ. Med.*, 2002, **59**, 708–711.
3 S. Antonaroli, B. Crociani, C. Di Natale, S. Nardis, M. Stefanelli and R. Paolesse, *Sens. Actuators, B*, 2015, **208**, 334–338.
4 A. Bhatt, V. Ravi, Y. Zhang, G. Heath, R. Davis and E. C. D. Tan, *J. Air Waste Manage. Assoc.*, 2023, **73**, 241–257.
5 X. Yao, Q. Yu, Z. Ji, Y. Lv, Y. Cao, C. Tang, F. Gao, L. Dong and Y. Chen, *Appl. Catal., B*, 2013, **130–131**, 293–304.
6 L. P. Teh, H. D. Setiabudi, S. N. Timmiati, M. A. A. Aziz, N. H. R. Annuar and N. N. Rulan, *Chem. Eng. Sci.*, 2021, **242**, 116606.
7 K. Yin, S. Mahamulkar, J. Xie, H. Shibata, A. Malek, L. Li, C. W. Jones, P. Agrawal and R. J. Davis, *Appl. Catal., A*, 2017, **535**, 17–23.
8 A. Longo, L. F. Liotta, G. Pantaleo, F. Giannici, A. M. Venezia and A. Martorana, *J. Phys. Chem. C*, 2012, **116**, 2960–2966.
9 T. Montini, M. Melchionna, M. Monai and P. Fornasiero, *Chem. Rev.*, 2016, **116**, 5987–6041.
10 P. Ebrahimi, A. Kumar and M. Khraisheh, *Catalysts*, 2022, **12**, 1101.
11 P. Biswas and D. Kunzru, *Int. J. Hydrogen Energy*, 2007, **32**, 969–980.
12 E. Prates da Costa, X. Huang, C. Kübel, X. Cheng, K. Schladitz, A. Hofmann, U. Göbel and B. M. Smarsly, *Langmuir*, 2023, **39**, 177–191.
13 C. R. Jung, J. Han, S. W. Nam, T.-H. Lim, S. A. Hong and H. I. Lee, *Catal. Today*, 2004, **93–95**, 183–190.
14 B. Wang, H. Zhang, W. Xu, X. Li, W. Wang, L. Zhang, Y. Li, Z. Peng, F. Yang and Z. Liu, *ACS Catal.*, 2020, **10**, 12385–12392.
15 S. Nassos, E. E. Svensson, M. Nilsson, M. Boutonnet and S. Järås, *Appl. Catal., B*, 2006, **64**, 96–102.
16 V. Bellière, G. Joorst, O. Stephan, F. M. F. de Groot and B. M. Weckhuysen, *J. Phys. Chem. B*, 2006, **110**, 9984–9990.
17 Y. Goto, M. Kikugawa, K. Kobayashi, T. Nanba, H. Matsumoto, K. Yamazaki, M. Matsumoto and H. Imagawa, *Chem. Commun.*, 2022, **58**, 3210–3213.
18 T. Kim, J. M. Vohs and R. J. Gorte, *Ind. Eng. Chem. Res.*, 2006, **45**, 5561–5565.
19 G. Balducci, P. Fornasiero, R. Di Monte, J. Kaspar, S. Meriani and M. Graziani, *Catal. Lett.*, 1995, **33**, 193–200.
20 P. Fornasiero, G. Balducci, J. Kašpar, S. Meriani, R. Di Monte and M. Graziani, *Catal. Today*, 1996, **29**, 47–52.
21 P. Li, X. Chen, Y. Li and J. W. Schwank, *Catal. Today*, 2019, **327**, 90–115.
22 H. S. Roh, H. S. Potdar, K. W. Jun, J. W. Kim and Y. S. Oh, *Appl. Catal., A*, 2004, **276**, 231–239.
23 W. S. Dong, K. W. Jun, H. S. Roh, Z. W. Liu and S. E. Park, *Catal. Lett.*, 2002, **78**, 215–222.
24 A. Konstandopoulos, C. Pagkoura, S. Lorentzou and G. Kastrinaki, *SAE Int. J. Engines*, 2016, **9**, 1709–1719.
25 D. Duprez, *Catal. Today*, 2006, **112**, 17–22.
26 S. Bedrane, C. Descorme and D. Duprez, *Catal. Today*, 2002, **73**, 233–238.
27 I. Iglesias, G. Baronetti and F. Marino, *Solid State Ionics*, 2017, **309**, 123–129.
28 J. Chen, B. Carlson, T. Toops, Z. Li, M. Lance, S. Karakalos, J. S. Choi and E. Kyriakidou, *ChemCatChem*, 2020, **12**, 5558–5568.
29 D. W. Lee, S. J. Kim, J. Lee, D. Yoo, Y. Kim, H. Kim, T. Chang, S. Kwon, I. Heo, Y. W. You and J. Lee, *Appl. Catal., A*, 2023, **663**, 119293.
30 L. Zhou, X. Li, Z. Yao, Z. Chen, M. Hong, R. Zhu, Y. Liang and J. Zhao, *Sci. Rep.*, 2016, **6**, 23900.
31 H. J. Kim, D. Shin, H. Jeong, M. G. Jang, H. Lee and J. W. Han, *ACS Catal.*, 2020, **10**, 14877–14886.
32 H. J. Kim, G. Lee, M. Jang, K. J. Noh and J. W. Han, *ChemCatChem*, 2019, **11**, 2288–2296.
33 M. Aryanpour, A. Khetan and H. Pitsch, *ACS Catal.*, 2013, **3**, 1253–1262.
34 F. Esch, S. Fabris, L. Zhou, T. Montini, C. Africh, P. Fornasiero, G. Comelli and R. Rosei, *Science*, 2005, **309**, 752–755.
35 A. Davo-Quinonero, E. Bailon-Garcia, S. Lopez-Rodriguez, J. Juan-Juan, D. Lozano-Castello, M. Garcia-Melchor, F. Herrera, E. Pellegrin, C. Escudero and A. Bueno-Lopez, *ACS Catal.*, 2020, **10**, 6532–6545.
36 S. Soni, N. Chouhan, R. K. Meena, S. Kumar, B. Dalela, M. Mishra, R. M. Meena, G. Gupta, S. Kumar, P. A. Alvi and S. Dalela, *Glob. Chall.*, 2019, **3**, 1800090.
37 L. Wang, K. Zhang, Z. Hu, W. Duan, F. Cheng and J. Chen, *Nano Res.*, 2014, **7**, 199–208.
38 P. C. Rath, J. Patra, D. Saikia, M. Mishra, J. K. Chang and H. M. Kao, *J. Mater. Chem. A*, 2016, **4**, 14222–14233.
39 C. Colbea, D. Avram, B. Cojocaru, R. Negrea, C. Ghica, V. G. Kessler, G. A. Seisenbaeva, V. Parvulescu and C. Tiseanu, *Nanomaterials*, 2018, **8**, 988.
40 C. C. Chen, W. Y. Cheng, S. Y. Lu, Y. F. Lin, Y. J. Hsu, K. S. Chang and K. L. Tung, *CrystEngComm*, 2010, **12**, 3664–3669.
41 A. Pophali, S. Singh and N. Verma, *Int. J. Hydrogen Energy*, 2020, **45**, 25985–25995.
42 P. M. V. Raja and A. R. Barron, *Physical methods in chemistry and nanoscience*, 2024, vol. 2, p. 55840, **https://chem.libretexts.org/Bookshelves/Analytical_Chemistry/Physical_Methods_in_Chemistry_and_Nano_Science_(Barron)/02%**

3A_Physical_and_Thermal_Analysis/2.03%3A_BET_Surface_Area_Analysis_of_Nanoparticles.
43 C. Oliveira, F. Garcia, D. Araujo, J. Macedo, S. Dias and J. Dias, *Appl. Catal., A*, 2012, **413–414**, 292–300.
44 L. Liu, B. Liu, L. Dong, J. Zhu, H. Wan, K. Sun, B. Zhao, H. Zhu, L. Dong and Y. Chen, *Appl. Catal., B*, 2009, **90**, 578–586.
45 Z. Wu, M. Li and S. H. Overbury, *J. Catal.*, 2012, **285**, 61–73.
46 K. Lee, B. Kim, J. Lee, G. Kwon, K. Yoon, H. Song, K. Min, S. Shim, S. Hwang and T. Kim, *Catal. Sci. Technol.*, 2024, **14**, 279–292.
47 K. Lee, M. Brito, J. DeCoster, K. Linskens, K. Mehdi, W. Lee, E. Kim, H. Kim, G. Kwon, C. Nam and T. Kim, *Mol. Catal.*, 2022, **528**, 112465.
48 K. Lee, G. Kwon, S. Hwang, J. A. Boscoboinik and T. Kim, *Catal. Sci. Technol.*, 2021, **11**, 7850–7865.
49 G. A. H. Mekhemer, *Colloids Surf., A*, 1998, **141**, 227–235.
50 P. E. Quintard, P. Barbéris, A. P. Mirgorodsky and T. Merle-Méjean, *J. Am. Ceram. Soc.*, 2004, **85**, 1745–1749.
51 T. Kaur, K. Singh and J. Kolte, *J. Phys. Chem. C*, 2022, **126**, 18018–18028.
52 Z. Wang, Y. Gao, Y. J. Chabal and K. Balkus Jr, *Catal. Lett.*, 2017, **147**, 738–744.
53 L. Li, F. Chen, J. Q. Lu and M. F. Luo, *J. Phys. Chem. A*, 2011, **115**, 7972–7977.
54 Y. Deng, A. D. Handoko, Y. Du, S. Xi and B. S. Yeo, *ACS Catal.*, 2016, **6**, 2473–2481.
55 G. Niaura, *Electrochim. Acta*, 2000, **45**, 3507–3519.
56 A. Singhal, M. R. Pai, R. Rao, K. T. Pillai, I. Lieberwirth and A. K. Tyagi, *Eur. J. Inorg. Chem.*, 2013, **2013**, 2640–2651.
57 L. Debbichi, M. C. Marco de Lucas, J. F. Pierson and P. J. Krüger, *J. Phys. Chem. C*, 2012, **116**, 10232–10237.
58 W. Wang, Z. Liu, Y. Liu, C. Xu, C. Zheng and G. Wang, *Appl. Phys. A: Mater. Sci. Process.*, 2003, **76**, 417–420.
59 N. Kainbayev, M. Sriubas, D. Virbukas, Z. Rutkuniene, K. Bockute, S. Bolegenova and G. Laukaitis, *Coatings*, 2020, **10**, 432.
60 K. C. Anjaneya, J. Manjanna, G. P. Nayaka, V. M. Ashwin Kumar, G. Govindaraj and K. N. Ganesha, *Phys. B*, 2014, **447**, 51–55.
61 V. V. Sal'Nikov and E. Pikalova, *Phys. Solid State*, 2015, **57**, 1944–1952.
62 S. Xu, A. Fan, H. Wang, X. Zhang and X. Wang, *Int. J. Heat Mass Transfer*, 2020, **154**, 119751.
63 C. Hess, *Chem. Soc. Rev.*, 2021, **50**, 3519–3564.
64 T. Taniguchi, T. Watanabe, N. Sugiyama, A. K. Subramani, H. Wagata, N. Matsushita and M. Yoshimura, *J. Phys. Chem. C*, 2009, **113**, 19789–19793.
65 T. Taniguchi, T. Watanebe, S. Ichinohe, M. Yoshimura, K. Katsumata, K. Okada and N. Matsushita, *Nanoscale*, 2010, **2**, 1426–1428.
66 B. M. Reddy and A. Khan, *Catal. Surv. Asia*, 2005, **9**, 155–171.
67 P. T. A. Campos, C. F. Oliveira, J. P. V. Lima, D. R. de Queiroz Silva, S. C. L. Dias and J. A. Dias, *J. Solid State Chem.*, 2022, **307**, 122752.
68 P. Chakartnarodom, N. Kongkajun and E. A. Laitila, *Key Eng. Mater.*, 2017, **751**, 202–206.
69 M. A. Thakar, S. S. Jha, K. Phasinam, R. Manne, Y. Qureshi and V. V. Hari Babu, *Mater. Today: Proc.*, 2022, **51**, 319–324.
70 S. Suresh, S. Karthikeyan and K. Jayamoorthy, *J. Sci.: Adv. Mater. Devices*, 2016, **1**, 343–350.
71 M. Ahamed, H. A. Alhadlaq, M. A. Majeed Khan, P. Karuppiah and N. A. Al-Dhabi, *J. Nanomater.*, 2014, **2014**, 637858.
72 C. Xie, D. Yan, H. Li, S. Du, W. Chen, Y. Wang, Y. Zou, R. Chen and S. Wang, *ACS Catal.*, 2020, **10**, 11082–11098.
73 C. Hu, Z. Zhang, H. Liu, P. Gao and Z. Wang, *Nanotechnology*, 2006, **17**, 5983–5987.
74 P. Shanmugam, G. P. Kuppuswamy, K. Pushparaj, B. Arumugam, A. Sundaramurthy and Y. Sivalingam, *J. Mater. Sci.: Mater. Electron.*, 2022, **33**, 9483–9489.
75 L. Zhou, X. Li, Z. Yao, Z. Chen, M. Hong, R. Zhu, Y. Liang and J. Zhao, *Sci. Rep.*, 2016, **6**, 23900.
76 S. Pengpanich, V. Meeyoo, T. Rirksomboon and K. Bunyakiat, *Appl. Catal., A*, 2002, **234**, 221–233.
77 L. Kurpaska, *J. Mol. Struct.*, 2018, **1163**, 287–293.
78 J. Chen, B. D. Carlson, T. J. Toops, Z. Li, M. J. Lance, S. G. Karakalos, J. S. Choi and E. A. Kyriakidou, *ChemCatChem*, 2020, **12**, 5558–5568.
79 O. Gorban, I. Danilenko, I. Nosolev, E. Abdullayev, A. Islamov, K. Gavrilenko, A. Doroshkevich, O. Shvets and S. Kolotilov, *J. Nanopart. Res.*, 2022, **24**, 197.
80 K. M. Lee, M. Brito, J. DeCoster, K. Linskens, K. Mehdi, W. I. Lee, E. Kim, H. Kim, G. Kwon, C.-Y. Nam and T. Kim, *Mol. Catal.*, 2022, **528**, 112465.
81 C. Deng, Q. Huang, X. Zhu, Q. Hu, W. Su, J. Qian, L. Dong, B. Li, M. Fan and C. Liang, *Appl. Surf. Sci.*, 2016, **389**, 1033–1049.
82 T. Naganuma and E. Traversa, *Nanoscale*, 2012, **4**, 4950.
83 F. Zhang, P. Wang, J. Koberstein, S. Khalid and S. Chan, *Surf. Sci.*, 2004, **563**, 74–82.
84 D. Barreca, A. Gasparotto and E. Tondello, *Surf. Sci. Spectra*, 2007, **14**, 41–51.
85 M. Ishfaq, M. Rizwan Khan, M. F. Bhopal, F. Nasim, A. Ali, A. S. Bhatti, I. Ahmed, S. Bhardwa and C. Cepe, *J. Appl. Phys.*, 2014, **115**, 174506.
86 B. M. Reddy, P. M. Sreekanth, Y. Yamada, Q. Xu and T. Kobayashi, *Appl. Catal., A*, 2002, **228**, 269–278.
87 D. Sotiropoulou and S. Ladas, *Surf. Sci.*, 1998, **408**, 182–189.
88 M. Park, J. Choi, L. Yang and H. Lee, *Sci. Rep.*, 2019, **9**, 19826.
89 J. Mucelini, R. Costa-Amaral, Y. Seminovski and J. L. F. Da Silva, *J. Chem. Phys.*, 2018, **149**, 244702.
90 V. Mastelaro, V. Briois, D. Souza and C. Silva, *J. Eur. Ceram. Soc.*, 2003, **23**, 273–282.
91 M. Gateshki, M. Niederberger, A. Deshpande, Y. Ren and V. Petkov, *J. Phys.: Condens. Matter*, 2007, **19**, 156205.
92 M. Kuhn, S. R. Bishop, J. L. M. Rupp and H. L. Tuller, *Acta Mater.*, 2013, **61**, 4277–4288.
93 T. Montini, M. Melchionna, M. Monai and P. Fornasiero, *Chem. Rev.*, 2016, **116**, 5987–6041.
94 A. Trovarelli and G. J. Hutchings, *Catalysis by Ceria and Related Materials*, Imperial College Press, 2002.

95 A. Adamski, P. Legutko, K. Dziadek, K. Parkhomenko, C. Aymonier, V. Sadykov and A.-C. Roger, *E3S Web of Conferences*, EDP Sciences, 2019, vol. 108.
96 C. Andriopoulou, D. Harris, H. Stephenson, A. Efstathiou and S. Boghosian, *Catalysts*, 2020, **10**, 462.
97 I. Dobrosz-Gómez, M. A. Garcia, M. I. Szynkowska, I. Kocemba and J. M. Rynkowski, *Catal. Today*, 2012, **191**, 142–145.
98 S. Wagloehner, D. Reichert, D. Leon-Sorezano, P. Balle, B. Geiger and S. Kureti, *J. Catal.*, 2008, **260**, 305–314.
99 I. Heo, S. J. Schmieg, S. H. Oh, W. Li, C. H. F. Peden, C. H. Kim and J. Szanyi, *Catal. Sci. Technol.*, 2018, **8**, 1383–1394.
100 M. Piumetti, S. Bensaid, D. Fino and N. Russo, *Appl. Catal., B*, 2016, **197**, 35–46.
101 S. Wagloehner, D. Reichert, D. Leon-Sorzano, P. Balle, B. Geiger and S. Kureti, *J. Catal.*, 2008, **260**, 305–314.
102 F. Zhao, S. Li, X. Wu, R. Yue, W. Li, X. Zha, Y. Deng and Y. Chen, *Catalysts*, 2019, **9**, 256.
103 K. An, S. Alayoglu, N. Musselwhite, S. Plamthottam, G. Melaet, A. E. Lindeman and G. A. Somorjai, *J. Am. Chem. Soc.*, 2013, **135**, 16689–16696.
104 D. Kim, D. Park, H. C. Song, B. Jeong, J. Lee, Y. Jung and J. Y. Park, *ACS Catal.*, 2023, **13**, 5326–5335.
105 C. H. Mejia, T. W. V. Deelen and K. P. D. Jong, *Nat. Commun.*, 2018, **9**, 4459.